Numerical study of turbulent flows around a cubic obstacle blown from a variable geometry jets diffuser

A. Fellague Chebra[a], M. Braikia[a], A. Khelil[a,*], M. Bedrouni[a], Z. Driss[b]

[a]*Control, Testing, Measurement and Mechanical Simulation Laboratory, University of Chlef, 2000 Chlef, Algeria*
[b]*Electro-Mechanic Systems Laboratory, National School of Engineers of Sfax, 3038 Sfax, Tunisia*

Abstract

This research focuses on utilizing numerical simulation to analyse how modifications in the air jet diffuser shape impact the cooling efficiency of electronic parts. The main aim of this study is to understand the physical and thermal mechanisms involved in the process. The study consists in numerically predicting the physical and thermal field of a cubic-shaped obstacle placed in the centre of a square subjected to a resulting flow field created by a transverse flow and a perpendicularly oriented impacting jet. The computations were done at a Reynolds number of 3 410, analyzing three perpendicular impinging jets with the ratio of impinging and cross flow Reynolds numbers $\alpha = \mathrm{Re}_j/\mathrm{Re}_H$ having the values of 0.5, 1, and 1.5. The k–ω SST turbulence model was used in this investigation. The effectiveness of the methodology that was put into action was evaluated by referring to the findings derived from the experiments conducted by Masip and his team. Once the methodology was validated, we studied the effect of changing the geometric shapes of the impinging jet diffusers on the cooling efficiency. Three geometrical shapes of air diffusers were tested (circular, swirling and lobed). We noted that there is a direct correlation between flow morphology and cooling efficiency. The impact of the ratio α was analysed and found to have a significant effect on the cooling efficiency. As this ratio increases, the quantity of heat transfer increases in all three air jet diffuser cases. In relation to the lobed air jet, it was observed that the Nusselt number exhibits greater values when compared to the other air jet diffuser cases. Moreover, it was noted that the lobed air jet diffuser can enhance the heat transfer efficiency for $\alpha = 1.5$ by more than 16.3 % compared to the circular air jet diffuser.
© 2024 University of West Bohemia.

Keywords: wall-mounted cube, cooling electronic components, impinging jet, circular jet, lobed jet, swirling jet

1. Introduction

The electronic components industry has undergone rapid expansion, resulting in a decrease in the size of electronic equipment designs. However, this reduction in size has led to a significant increase in the amount of heat generated by such equipments. A predominant cause of electronic component failures is commonly attributed to thermal overheating. An optimal cooling system is imperative to ensure effective cooling and prevent potential hardware impairment. In contemporary industrial settings, the investigation and enhancement of cooling methodologies for electronic components are gaining greater significance. The primary aim of the cooling process is to guarantee that electronic components operate within a secure environment by several approaches. For example, the utilization of a heat pipe, a heat sink with fins, or the implementation of confined impinging jets can be considered. Enhancing the efficiency of cooling in different categories of electronic systems and other portable heat-dissipating apparatuses persistently presents a notable obstacle [4] and [39].

Nomenclature

LHV	lower horseshoe vortex	S_{ij}	strain rate tensor [s^{-1}]
UHV	upper horseshoe vortex	T	mean temperature [K]
SV	side vortex	U_H	inlet cross flow velocity [m s^{-1}]
WV	wake vortex	U_J	inlet jet velocity [m s^{-1}]
D	diffuser jet diameter [m]	x, y, z	Cartesian coordinates [m]
H	channel height [m]	y^+	dimensionless wall distance [–]
h	cube height [m]	δ_{ij}	Kronecker delta [–]
k	turbulent kinetic energy [m^2 s^{-2}]	Ω_{ij}	antisymmetric vortex tensor [s^{-1}]
Nu	Nusselt number [–]	ω	turbulent frequency [s^{-1}]
P	pressure [Pa]	μ	dynamic viscosity [kg m^{-1} s^{-1}]
P_k	production terms of k	μ_t	turbulent viscosity [kg m^{-1} s^{-1}]
Pr$_t$	turbulent Prandtl number [–]	ϱ	density [kg m^{-3}]
q	heat flux [W]	λ	thermal conductivity [W m^{-1} K^{-1}]
Re$_H$	cross flow Reynolds number [–]	α	Reynolds number ratio [–]
Re$_j$	impinging flow Reynolds number [–]		

Impinging jets are commonly utilized in various practical applications, including ventilation, cooling, tempering, and shaping of glass, and drying textiles. Additionally, these jets are employed in anti-icing processes of aircraft wings and engine in-lets, as well as the cooling of turbine blades and electronic components, as cited in the literature [4, 8, 25]. Various experimental and numerical studies dealing with impinging jets have been presented in the literature. Typically, these studies focus on the impact of specific parameters, such as fluid choice, blow diffuser geometry, selected turbulence models, Reynolds number and electronic element geometry, on enhancing heat transfer. Some of the related studies are provided below.

In their research [42], Xu et al. conducted a numerical investigation into the flow characteristics that occur within jet pumps with distinct nozzle cross-sections. The investigators employed the realizable k–ε model and the wall function, based on the finite volume method, to carry out their numerical study. The research findings indicate that a square shape diffuser exhibits a maximum efficiency that surpasses that of both the circular and triangular diffusers by 3 % and 4.1 %, respectively. The authors have observed that the utilization of non-circular nozzles results in a reduction in recirculation area and friction loss in comparison to conventionally used circular nozzles, along with an enhancement in the mixing effect. According to Khelil et al. [18], a finite volume methodology was utilized to perform a numerical analysis of multiple swirling jets. The turbulence was simulated by applying two distinct modelling techniques, namely the standard k–ε model and the Reynolds stress model (RSM). It was reported that the functional consistency of the RSM numerical outcomes with the empirical data was superior. Additional findings demonstrated that the optimal angle of the diffuser vanes, along with a precise temperature regulation between central and peripheral jets, significantly affects the efficiency of thermal homogenization, with particular regard to swirl angles. In [22], Lee conducted a comparative investigation into the disintegration properties of pneumatic diffusers that are internally mixed, whilst considering multiple operating conditions. For the purpose of enhancing the pneumatic jets mixing capabilities, an investigation was conducted on four swirling internal mixing nozzles. These nozzles were equipped with axisymmetric orifices that displayed distinct swirl angles ranging from 15° to 60° relative to the centre axis. It was ob-

served that the atomization characteristics exhibited favorable performance when subjected to a vortex angle of 30°. Furthermore, a decline in the intensity of turbulence was noted steadily as the azimuthal distance increased. It was demonstrated that the geometric parameter of the nozzle configuration plays a significant role in influencing the trajectory of the jet. Thundil Karuppa Raj and Ganesan [36] highlighted the main characteristics of the flow field produced by the swirling jet. The originality of the research lies in identifying the optimum diffuser vane angle through the use of relevant turbulence models for weak and strong eddies. This will create a unique addition to the existing information, which will be a valuable contribution. It was established that the standard k–ε model is appropriate in situations involving weak vortices. In situation with powerful vortices, the RSM use is deemed necessary. The findings of the current investigation have ascertained that within the range of blade angles assessed, the optimal blade angle is 45°.

In [26], Meslem et al. conducted a study to examine the efficiency of three turbulence models, namely the standard k–ε model, the shear stress transport (SST) k–ω model, and the RSM. The researchers noted that no turbulence models have demonstrated optimal accuracy in predicting all flow characteristics. Recent research has demonstrated that, within the scope of investigated viscous models, the k–ω SST turbulence model exhibits a commendable ability to effectively forecast jet interaction, wide-ranging dynamic expansion, as well as the entrainment of ambient air in relation to the volume flux emanating from a lobed diffuser. In the field of fluid dynamics, Meslem and Nastase [27] have conducted an investigation on an isothermal turbulent air jet that is produced by means of a lobed nozzle. The experimental findings were contrasted with those of a circular jet having equivalent axisymmetric characteristics and initial parameters. The authors have revealed that the high entrainment rate is attributable to turbulent structures generated by the lobes in conjunction with the asymmetrical nozzle geometry that instigates vigorous convection. In the study [6] by Bennia et al., a comparison was conducted on the performance of various lobed nozzle geometries. The researchers conducted an examination of the lobed jet by using diverse lobe geometries and performed an analysis on the axial velocity profiles of the jet. The findings reveal that an inclined lobed diffuser facilitates greater homogenization of airflow in the experimental space compared to a lobed diffuser featuring a uniform, straight section.

In their experimental research [38], Tummers et al. investigated the characteristics of flow structure and temperature distribution in the vicinity of a cube's wall. The configuration of the cubes within this experimental setup involved a linear arrangement comprising of five individual cubes. The aforementioned structures were explicitly introduced into the lowermost surface area of the channel with a perpendicular impinging jet point. The study [38] employed particle image velocimetry (PIV) as a tool for the measurement of turbulent flow around the cubes, whilst the distribution of temperature was carried out in a simultaneous manner by employing an infrared imaging system. Upon conducting experiments utilizing two distinct impact jet positions, a complex flow structure was uncovered. Remarkably, this structure entailed the generation of several intricate flow features such as vortices, recirculation zones, slowing regions, stagnation points, separations and curvature effects. These phenomena had a discernible impact on the temperature distribution along the surfaces of the cube. In [28], Ostheimer and Yang simulated a double impinging jet in cross flow and found that both the k–ε model and the RSM predicted the mean velocity profiles reasonably well. RSM exhibited a modest enhancement in predictive capability. They noted that the RSM Reynolds stress prediction was poor compared to experimental data, highlighting the need for a large eddy simulation (LES) to capture unsteady flow details.

In [32], Rundström and Moshfegh conducted a numerical exploration of the interaction between an impinging jet and a low velocity channel flow. The study concerned the analysis of a channel configuration that included a centrally positioned cube that is heated on the base plate, in addition to two separate inlets. One inlet enabled horizontal channel flow, while the other facilitated vertical impinging jet flow. The study assessed the effectiveness of the RSM as a turbulence model by means of computational simulations and investigated the influence of the jet Reynolds number and the jet-to-cross-flow velocity ratio on the aerodynamic and surface temperature features encompassing a cube. Additionally, the study intended to analyze the average values and localized distributions of the heat transfer coefficient. An experimental assessment was carried out by Choo et al. in [10] in order to examine the thermal features of inclined impinging jets. According to the findings posited by the authors, one may infer that the heat transfer process is greatly influenced by the gap between the impinging jet and the plate. The investigators have determined that the location of the jet in close proximity resulted in heightened impact points and raised Nusselt numbers on average. However, it is noteworthy that an increase in the distance of jet placement resulted in a corresponding decrease in both the average Nusselt number and the impact point while the inclination angle also underwent a concurrent rise. This trend was observed and should be taken into consideration when analyzing the results.

In [40], Wang et al. delved into an investigation of the influence of vortex generators on a transverse flow jet with the aid of experimental techniques. A primary focus was afforded towards exploring the impact of Reynolds number fluctuations across diverse conditions. The authors maintained a constant Reynolds number of 15 000 for the jet while examining the Reynolds number of the cross flow, which varied between 40 000 and 64 000. It was determined that the augmentation of heat transfer is dependent upon the configuration and altitude of the vortex generators, in combination with the cross flow Reynolds number. Numerical predictions were carried out by Ajmi et al. in [1], where the k–ω SST turbulence model was employed to examine a heated jet that was both tilted and offset. The authors presented the Nusselt evolution at a local level for varying combinations of the Reynolds number, offset ratio, and tilt angle in order to elucidate their collective influence on convective transfer. The utilization of such correlations harbors the potential for the augmentation of current scientific understanding and enhancement of heat transfer in an assortment of engineering domains, encompassing, inter alia, heat exchange systems deployed in the context of electronics cooling.

The LES method was used by Popovac and Hanjalić in [30] for a computational procedure. The investigation was based on the use of a thermally activated cube, located in a pipe having a vertically directed orthogonal jet. The temperature of the heated cube underwent a cooling process that involved a combination of air, a channel flow characterized by a Reynolds number of 4 800, and a circle jet with a Reynolds number of 5 200. The primary aim of the study was to analyze the different flow structures and turbulence statistics, while also investigating the heat transfer properties on the area of a cubic-shaped structure. The results obtained through simulation were subjected to comparison with experimental measurements, which revealed a degree of qualitative correspondence tempered by observing substantial deviations in the flow conditions. In [23], Masip et al. studied turbulent flow near a cube attached to a wall in a conduit experiencing cross-flow and incident jet interactions. The study tested cross flow at three Reynolds numbers ($\mathrm{Re}_H = 3\,410, 5\,752,$ and $8\,880$) and different ratios $\alpha = \mathrm{Re}_j/\mathrm{Re}_H$, i.e., nine cases were studied. The authors used PIV to measure velocity across planes, determining mean velocity and Reynolds stresses. They found that the Reynolds number ratio α had a greater effect on flow behavior than the Reynolds number of the transverse flow (Re_H). In the case of

a smaller ratio, the jet had drag forces but no impact on the component. The authors analyzed flow morphology and phenomena across all nine cases.

The effect of turbulence on the development of cube's wake located close to a wall have been examined by Hearst et al. in [12]. The authors created turbulent boundary layers with varying levels of turbulence while keeping shear profiles comparable. They found that the stagnation and attachment points on the cube remained unchanged despite the changes to the incoming profile. The authors observed that the turbulence increases and shortens the wake length while normalized shear remains constant. In [34], Saleha et al. analyzed the chamfering effect on cube cooling efficiency using the k–ω SST model at a Reynolds number of 3 410. Three Reynolds number ratios (0.5, 1 and 1.5) were tested in this study. No improvement has been seen for the first two ratios, but a 26% increase was observed for the cube with 4 mm chamfer at the highest ratio 1.5. Bedrouni and Khelil [4] researched the impact of rounded electronic component corners on cooling in cross flow and impinging jets, simulating for $\alpha = 0.5$, 1, and 1.5. Reynolds-averaged Navier-Stokes (RANS) simulations showed that an increasing Reynolds number ratio improves heat flux in all cube geometries. The implementation of rounded top corners was found to significantly improve the cooling effectiveness of cube-shaped objects. Specifically, for α values of 1 and 1.5, this technique resulted in enhancements of 6 % and 23 %, respectively, in comparison to conventional cubes. The k–ω SST model generated rational results for the mean streamwise velocities.

In [2], Albayrak et al. studied how the jet velocity ratio affects flow patterns and heat transfer in a heated channel resembling electronic components. The study used numerical simulations to compare different velocity ratios and their impact on heat transfer. Once the jet momentum exceeds that of the transverse flow, there is a noticeable increase in heat transfer by convection, which causes the heat enhancement factor to rise. This factor depends on the ratio of jet velocity and cross flows, illustrating their impact on heat transfer by convection. Greater velocity of the jet results in enhanced thermal performance. Rakhsha et al. [31] explored the impact of nozzle geometry on flow and heat transfer from a pulsed jet onto a concave surface. Experimental trials employed a circular jet, while numerical simulations encompassed circular, elliptical, rectangular, and square geometries. Findings revealed that nozzle shape directly influences air entrainment and the average Nusselt number $\mathrm{Nu_{ave}}$. Pulsating the jet at 100 Hz resulted in a 20% increase in $\mathrm{Nu_{ave}}$ for circular/square jets and in a 15% increase for elliptical/rectangular jets. Generally, pulsation either reduced or increased $\mathrm{Nu_{ave}}$ at low and high frequencies, respectively, compared to steady jets. In [17], Khan and Saha conducted an investigation into turbulent jet and thermal transfer of an impinging jet over a three-dimensional object in cross flow, employing the LES technique. They utilized the finite volume method for the Navier-Stokes and energy equations, maintaining constant Reynolds and Prandtl numbers. Their results indicated that the heat transfer at a cuboid upper surface and lateral surfaces improves, although the rear surface experiences a minor loss. They also carried out a numerical simulation to compare the turbulent thermal transfer on a heated cube without an impinging jet.

Using the impinging jet technology in [15], Karabulut quantitatively investigated the enhancement of convective heat transfer from copper plate patterned surfaces. The research addressed the thermal load of microchips and utilized the Ansys Fluent software with the k–ε turbulence model. Various Reynolds numbers and jet-to-plate distances were considered, examining different patterned surfaces within rectangular channels. Consistent with previous studies, the straight-circle-patterned surfaces exhibited a 24.13% higher mean Nusselt number compared to the reverse-circle-patterned surfaces at $\mathrm{Re} = 10\,000$ and $H/D_h = 12$. In his second study [16], Karabulut investigated heat transfer and flow characteristics in channels

with cross-flow-impinging jet-flow, focusing on a cube and circular hollow models using water and 2% CuO-water nanofluid. Numerical simulations included fin additions with 45° and 90° angles at varying lengths on the top channel surface, conducted with Ansys Fluent and the k–ε turbulence model. A constant heat flux of $1\,000\,\mathrm{W\,m^{-2}}$ was applied and the 3D channel height remained fixed. The Reynolds numbers ranged from $5\,000$ to $15\,000$. The numerical results of the study aligned well with experimental data. Evaluation parameters encompassed the mean Nusselt number, surface temperature, and performance coefficient variations. Specifically, the average Nusselt number increased by 32.55 % and 26.11 % for the CuO-water nanofluid at Re $= 15\,000$, $K = D$, and a 90° fin angle, respectively, compared to the cube and circular hollow models without fins and with fluid (water).

According to the findings of the literature review, a noticeable lack of attention has been paid to the impact of impinging jet forms on cooling efficiency. The present study aims to examine and clarify the impacts of three different types of impinging jet diffusers, namely circular, lobed and swirling, confronted with cross flow, with particular emphasis placed on their cooling efficiency.

2. Governing equations and turbulent modeling

2.1. Problem definition and boundary conditions

The presented research involves an electronic component in the shape of a cube that is placed at the geometric center of a square channel and is exposed to the effects of a transverse flow and a perpendicular impinging jet. The employed configuration exhibits resemblance to the experimental conditions reported by Masip et al. in [23]. The present study seeks to verify the accuracy of our numerical results by means of comparison with the results obtained through experimentation. Fig. 1 depicts an illustration of the computational domain, relevant boundary conditions included. The vertical dimension of the component is indicated as $h = 15\,\mathrm{mm}$. The horizontal extent of the channel, as measured along the x-axis, is set to a value of $20h$, where h corresponds to the height of the cubic form. The width of the channel is $15h$, while the height of the domain, which is represented on the y-axis, equals to $2h$. Incompressible air is used as the cooling medium with a temperature of $293\,\mathrm{K}$. The current investigation was conducted under a constant Reynolds number indicative of cross flow, specifically designated as $\mathrm{Re}_H = 3\,410$. This value was accurately determined in relation to the inlet velocity ($U_H = 1.705\,\mathrm{m\,s^{-1}}$) and was calculated with the channel height set at $H = 2h$. Additionally, the component underwent exposure to a perpendicular impinging jet, characterized by three distinct velocities ($U_j = 2.131\,3$, $4.262\,5$, and $6.393\,8\,\mathrm{m\,s^{-1}}$) and corresponding Reynolds numbers ($\mathrm{Re}_j = 1\,705$, $3\,410$, and $5\,115$). The impinging jet can take various forms, such as a circular jet, lobed jet, and swirling jet. The study delves into three distinct Reynolds number ratios between the impinging jet and the channel flow ($\alpha = \mathrm{Re}_j/\mathrm{Re}_H = 0.5$, 1, and 1.5). The inlet boundary conditions consisting of channel flow and impinging jet are applied with a thermal input of 293 K. At the exit of the system, a relative pressure boundary condition is applied, where the outlet pressure is maintained at $0\,\mathrm{Pa}$. The present study considers smooth, slip-free walls as the remaining boundaries with a uniform temperature equal to the temperature of the fluid (i.e., 293 K), except in the case of the heated cube where the temperature has been established at 348 K. Table 1 presents a comprehensive overview of additional information.

Table 1. Parameters and conditions employed to simulate the phenomenon concerning its boundaries

Type of simulation	three-dimensional (3D) steady jet
Model of turbulence	k–ω SST
Criterion of convergence	10^{-5}
CFD code	Ansys Fluent
Height of the cube	$h = 15\,\text{mm}$
Cross flow Reynolds number	$\text{Re}_H = 3\,410$
Reynolds number ratios	$\alpha = \text{Re}_j/\text{Re}_H = 0.5, 1 \text{ and } 1.5$
Cylinder diameter	$D = 12\,\text{mm}$
Input cross flow	$U_H = 1.705\,\text{m s}^{-1} \text{ and } T = 293\,\text{K}$
Outlet	$P_{out} = 0\,\text{Pa}$
All walls	No-slip walls, i.e., $U = 0\,\text{m s}^{-1}$
Channel walls temperature	$T = 293\,\text{K}$
Cube walls temperature	$T = 348\,\text{K}$
Dynamic viscosity	$\mu = 1.837\,5 \times 10^{-5}\,\text{kg m}^{-1}\,\text{s}^{-1}$
Fluid density	$\varrho = 1.225\,\text{kg m}^{-3}$
Thermal conductivity	$\lambda = 0.024\,2\,\text{W m}^{-1}\,\text{K}^{-1}$
Specific heat capacity	$C_p = 1\,006.43\,\text{J kg}^{-1}\,\text{K}^{-1}$
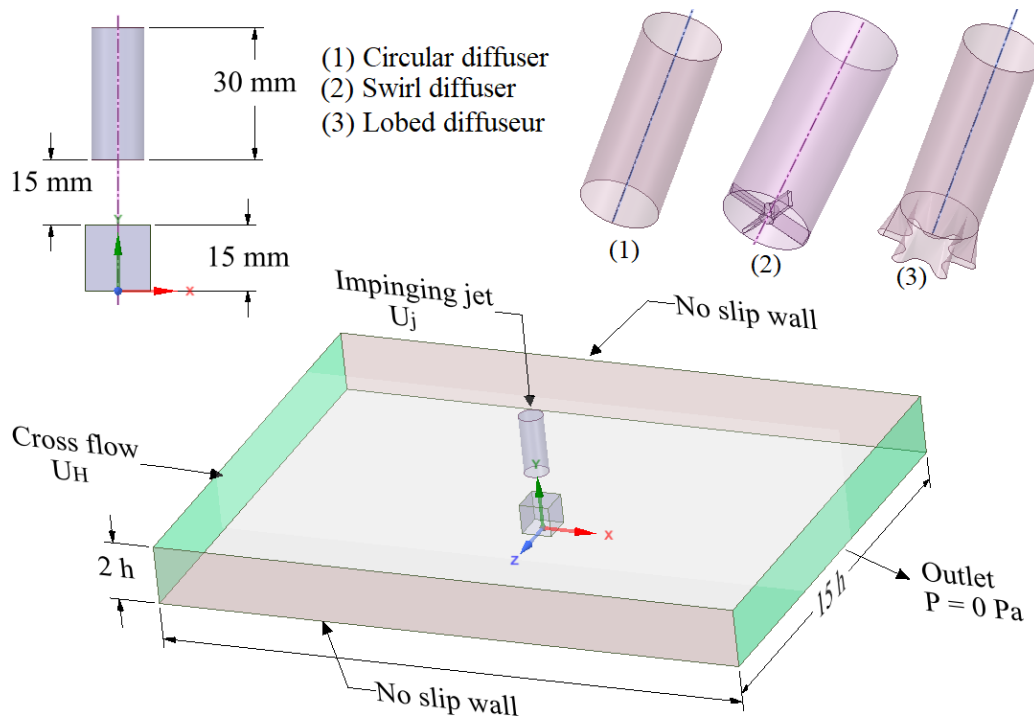
Fig. 1. Schematic illustration of the computational space with its limitations, such as boundary conditions

Circular jet

Fig. 2 illustrates the geometric configuration of the circular diffuser used in the present investigation. The diffuser consists of a circular tube measuring 12 mm in diameter and 30 mm in
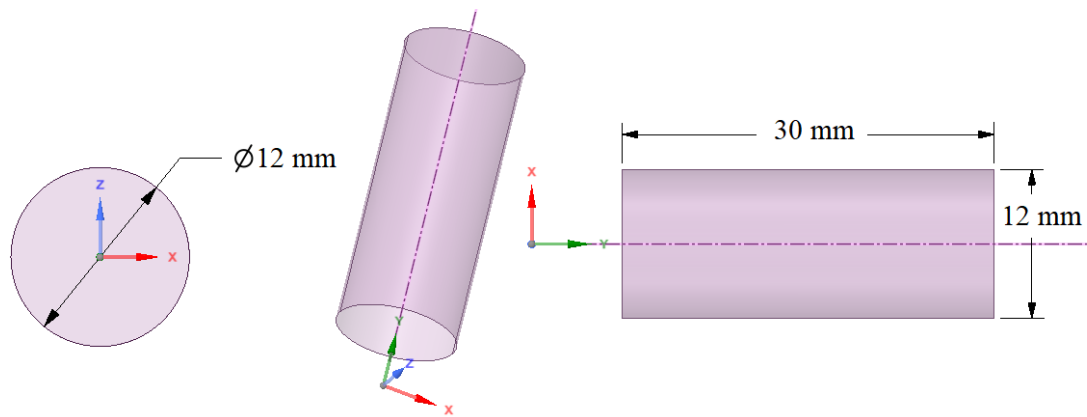
Fig. 2. Circular diffuser geometry

length. The obstacle has a cubic geometric shape with a dimension of $15 \times 15 \times 15$ mm. The distance between the diffuser and the obstacle is fixed at $H = 15$ mm.

Lobed jet

The geometry of the lobed diffuser employed in this research is presented in Fig. 3. The diffuser is comprised of a circular tube with a diameter of $D = 12$ mm and equipped with a daisy-shaped configuration at its outlet. Six lobes inclined at an angle and exhibiting parallel sides, as well as six sinusoidal troughs characterize the exit plane. The inner and outer penetration angles, denoted by $\theta_{in} = 22°$ and $\theta_{out} = 14°$, respectively, were evaluated. The measurements of each lobe include a length H of 6 mm and a height W of 1.8 mm.
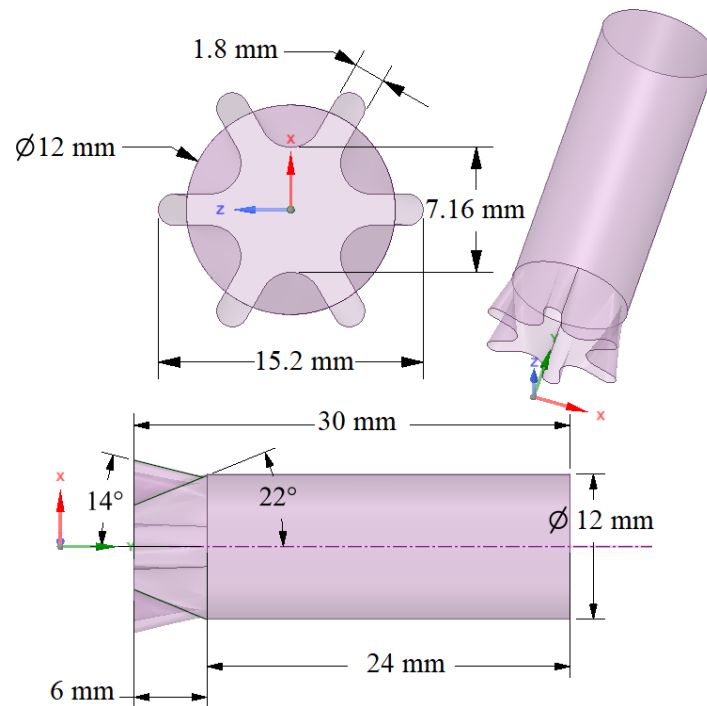
Fig. 3. Lobed jet diffuser geometry
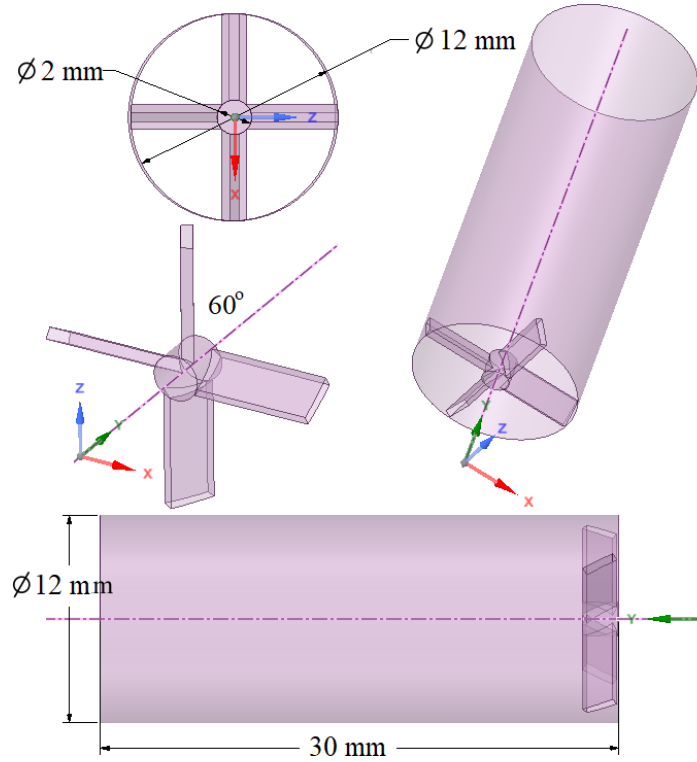
Fig. 4. Swirl diffuser geometry

Swirling jet

Fig. 4 illustrates the geometric configuration of the swirl diffuser employed in this study. The diffuser is comprised of a circular tube with a diameter $D = 12\,\text{mm}$ and a length of $30\,\text{mm}$. It is equipped with four fins inclined at an angle of $60°$ relative to the central axis.

2.2. Turbulence modeling

The present investigation assumes that the fluid under consideration is incompressible and that the flow is presumed to be steady. The equations governing the continuity and momentum of fluid flow, commonly referred to as the Reynolds-averaged Navier-Stokes (RANS) equations, are expressed in differential form and can be conveniently represented via tensor notation [3, 7, 11, 19, 20]

$$\frac{\partial U_i}{\partial x_i} = 0, \tag{1}$$

$$\varrho \frac{\partial (U_i U_j)}{\partial x_j} = -\frac{\partial P}{\partial x_i} + \frac{\partial}{\partial x_j} \left[\mu \left(\frac{\partial U_i}{\partial x_j} + \frac{\partial U_j}{\partial x_i} \right) - \varrho \overline{u_i' u_j'} \right], \tag{2}$$

$$\varrho\, C_p U_i \frac{\partial T}{\partial x_i} = \frac{\partial}{\partial x_i} \left(\lambda \frac{\partial T}{\partial x_i} - \varrho\, C_p \overline{u_i' T'} \right). \tag{3}$$

Here, the mean velocity and temperature are represented by U_i and T, respectively, while the other parameters include μ for the dynamic viscosity, ϱ for the fluid density, P for the mean pressure, C_p for the specific heat capacity at constant pressure, λ for the thermal conductivity, u_i', u_j' and T' for the corresponding fluctuation components, $-\varrho\,\overline{u_i' u_j'}$ and $-\varrho\,C_p\,\overline{u_i' T'}$ for the average Reynolds stresses and turbulent heat fluxes. To obtain a complete set of equations, models for

$-\varrho \, \overline{u_i' u_j'}$ and $-\varrho \, C_p \, \overline{u_i' T'}$ are required to close the equations, as discussed in [4, 9, 21, 35]. The channel walls and cube faces are assumed to adhere to a no-slip condition, i.e.,

$$U = 0|_{\text{walls}}. \tag{4}$$

This work employs the k–ω SST model, where the Boussinesq approximation describes the linear relationship between the Reynolds stress and the strain rate as [41]

$$-\varrho \, \overline{u_i' u_j'} = \mu_t \left(2S_{ij} - \frac{2}{3} \frac{\partial U_k}{\partial x_k} \delta_{ij} \right) - \frac{2}{3} \varrho k \delta_{ij}, \qquad S_{ij} = \frac{1}{2} \left(\frac{\partial U_i}{\partial x_j} + \frac{\partial U_j}{\partial x_i} \right), \tag{5}$$

where k denotes the turbulent kinetic energy, δ_{ij} represents the Kronecker delta, and the turbulent viscosity μ_t is defined as

$$\mu_t = \varrho \nu_t = \frac{a_1 \varrho k}{\max \left(a_1 \omega, f_2 S \right)}, \tag{6}$$

where $S = \sqrt{2S_{ij}S_{ij}}$ is the invariant measure of the strain rate, and ω is the turbulent frequency. Through the use of the Boussinesq approximation, a model that presumes the proportionality between the turbulent heat flux and the turbulent viscosity, turbulent thermal flows can be represented by the following equation [5, 29]:

$$-\varrho \, \overline{u_i' T'} = \frac{\mu_t}{\text{Pr}_t} \frac{\partial T}{\partial x_i}. \tag{7}$$

The turbulent Prandtl number, denoted by Pr_t, is a parameter used to evaluate turbulence mixing efficiency and is set to $\text{Pr}_t = 0.85$ for this study. The k–ω SST turbulence model, developed by Menter in [24], is widely used due to its accurate representation of flow physics and numerical stability. This model is a combination of the k–ε and standard k–ω models and its formulation can be found in [13, 15, 33, 37]

$$\frac{\partial(\varrho k)}{\partial t} + \frac{\partial(\varrho U_j k)}{\partial x_j} = \overline{P}_k - \beta^* \varrho \omega k + \frac{\partial}{\partial x_j} \left[(\mu + \sigma_k \mu_t) \frac{\partial k}{\partial x_j} \right], \tag{8}$$

$$\frac{\partial(\varrho \omega)}{\partial t} + \frac{\partial(\varrho U_j \omega)}{\partial x_j} = \frac{\phi}{\nu_t} \overline{P}_k - \beta \varrho \omega^2 + \frac{\partial}{\partial x_j} \left[(\mu + \sigma_\omega \mu_t) \frac{\partial \omega}{\partial x_j} \right] + 2(1 - f_1) \frac{\varrho \sigma_{\omega 2}}{\omega} \frac{\partial k}{\partial x_j} \frac{\partial \omega}{\partial x_j}, \tag{9}$$

$$P_k = \mu_t \frac{\partial U_i}{\partial x_j} \left(\frac{\partial U_i}{\partial x_j} + \frac{\partial U_j}{\partial x_i} \right), \qquad \overline{P}_k = \min \left(P_k, 10\beta^* \varrho k \omega \right), \tag{10}$$

where f_1 and f_2 are the blending functions computed using the following expressions:

$$f_1 = \tanh \left(\Gamma_1^4 \right), \qquad f_2 = \tanh \left(\Gamma_2^2 \right). \tag{11}$$

The effectiveness of diffusivity, Γ_1 and Γ_2, can be expressed as

$$\Gamma_1 = \min \left[\max \left(\frac{\sqrt{k}}{\beta^* \omega d}, \frac{500\nu}{\omega d^2} \right), \frac{4\varrho \sigma_{\omega 2} k}{CD_{k\omega} d^2} \right], \qquad \Gamma_2 = \max \left(\frac{2\sqrt{k}}{\beta^* \omega d}, \frac{500\nu}{\omega d^2} \right), \tag{12}$$

where d is the distance to the nearest wall and $CD_{k\omega}$ represents the positive portion of the cross-diffusion term, which is derived from the following equation:

$$CD_{k\omega} = \max \left(2\varrho \sigma_{\omega 2} \frac{1}{\omega} \frac{\partial k}{\partial x_j} \frac{\partial \omega}{\partial x_j}, 10^{-10} \right). \tag{13}$$

All constants are calculated as a blend of the corresponding constants from the k–ε and the k–ω models using the formula: $\phi = f_1\phi_1 + (1 - f_1)\phi_2$, where ϕ_1 and ϕ_2 are the constants from the k–ε and k–ω models, respectively. According to [24], the constants for the model are

$$\beta^* = 0.09, \qquad \phi_1 = \frac{5}{9}, \qquad \beta_1 = 0.075, \qquad \sigma_{k1} = 0.85, \qquad \sigma_{\omega1} = 0.5,$$

$$\phi_2 = 0.44, \qquad \beta_2 = 0.082\,8, \qquad \sigma_{k2} = 1, \qquad \sigma_{\omega2} = 0.856, \qquad a_1 = 0.31.$$

The local Nusselt number can be obtained using the following equation:

$$\mathrm{Nu} = \frac{hq}{\lambda\,(T_w - T_b)}, \tag{14}$$

where T_w and T_b denote the local temperature of the heated cube and the local bulk temperature of the fluid, respectively, while q represents the heat flux.

2.3. Meshing process description

The convergence of the simulations greatly relies on the quality of the mesh. Careful mesh generation is essential to obtain rapid and requested simulation convergence. The mesh exhibited non-uniformity as evidenced by its high density allocation in regions of significant gradient variation and conversely, low density allocation in regions of comparative insignificance. This strategic allocation of mesh density served the dual purpose of minimizing computational effort while ensuring an adequate level of precision, as documented by references [4] and [18]. In the present investigation, a carefully designed hexahedral mesh is employed for the simulations, which is generated by means of the Ansys ICEM software. The mesh generated within the computational domain is depicted in Fig. 5a. In Fig. 5b, the mesh in the proximity of the diffuser is displayed. Fig. 5c displays the mesh in the proximity to the cubic surface of the domain. In order to address the issue of boundary layer separation, exceedingly small meshes have been introduced in close proximity to both the walls and the cube.

In this study, four distinct meshes characterized by various mesh sizes were analyzed to ascertain the degree of the solution independence in relation to both mesh quality and number of nodes. For this purpose, circular jet simulations were conducted. Table 2 provides a comprehensive overview of these structures, all of which are characterized by a hexahedral form.

It is noteworthy that the mean Nusselt number is found to be contingent on the mesh dimensions in instances 1, 2, 3, and 4. Nevertheless, both the y^+ parameter and the average Nusselt number exhibit minimal changes as the mesh size increases. The present study employs Mesh 4 for the purpose of effectively capturing the laminar and transient boundary layers. This refinement near the walls resulted in a maximum value of $y^+ = 0.2$ for the cube and $y^+ = 0.8$ for the walls, as shown in Fig. 6. Here, $y^+ = u_t y/\nu$ is the dimensionless distance of a cell from

Table 2. Characteristics of the different meshes for the chosen configuration

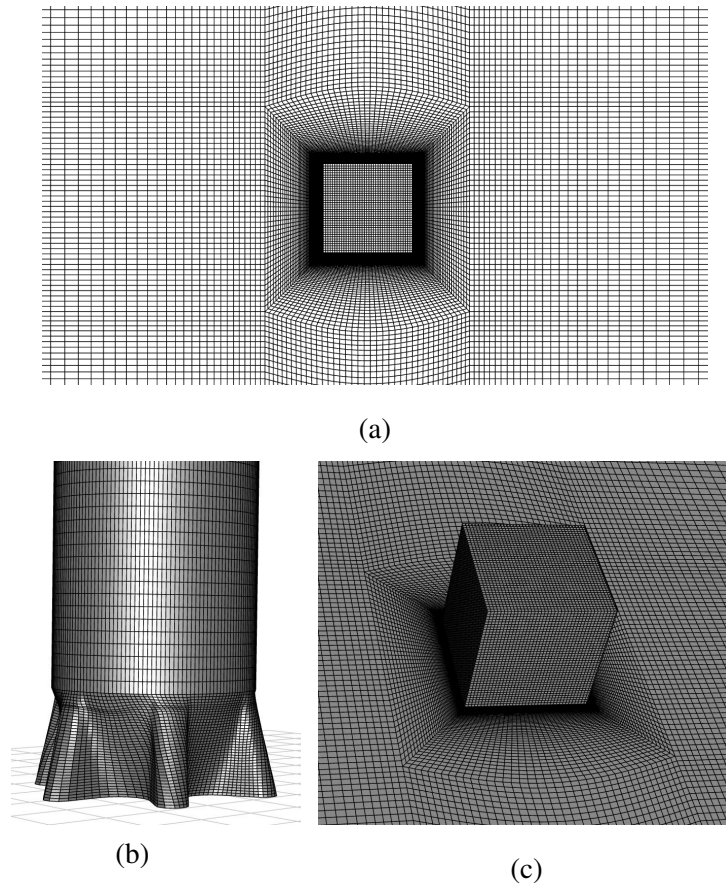| Mesh	Number of nodes	Average y^+	Mean Nusselt number
Mesh 1	527 006	2.708	26.42
Mesh 2	1 229 446	0.500	25.76
Mesh 3	2 629 436	0.460	25.59
Mesh 4	3 410 021	0.292	25.49

(a)

(b)

(c)

Fig. 5. Mesh topology: (a) domain mesh, (b) mesh near the diffuser, (c) mesh near the cube

the wall, where u_t is the friction velocity, y is the distance to the nearest wall measured in the normal direction, and ν is the fluid kinematic viscosity [8]. Calculations were conducted for all geometrical instances (circular, lobed, and swirl), utilizing a mesh size of $3\,410\,021$ nodes.

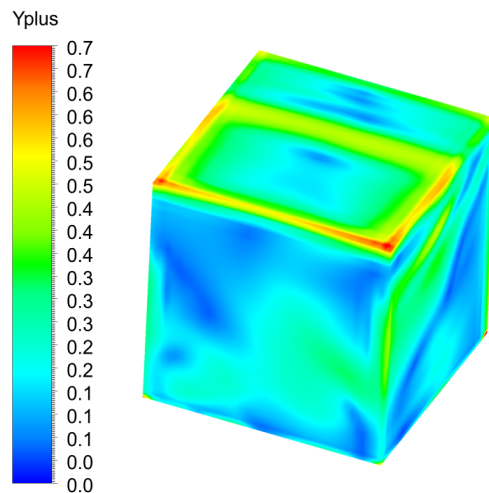Fig. 7 illustrates transverse velocity profiles in the flow direction for various mesh sizes,

Fig. 6. Values of y^+ at a cell above the cube surface
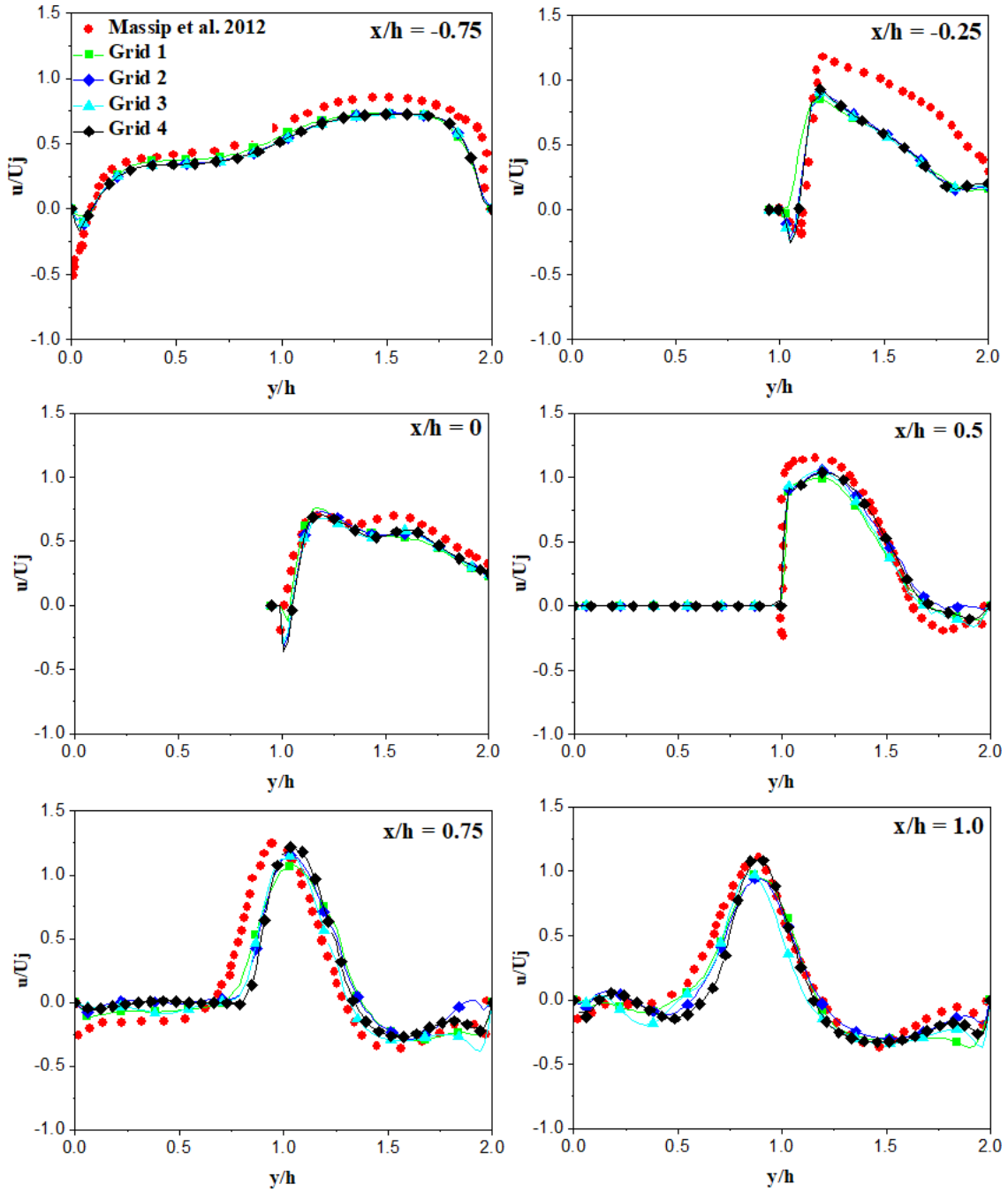
Fig. 7. Transverse velocity profiles in the flow direction for different mesh sizes compared to experimental data from [23] at selected axial locations and $z = 0$, $\alpha = 0.5$

alongside experimental data at selected axial points. Overall, the calculated transverse velocity profiles align well with the experimental data at virtually all locations, with Mesh 4 showing superior agreement compared to the other meshes. The root mean square error (RMS) was computed for $\alpha = \mathrm{Re}_j / \mathrm{Re}_H = 0.5$, as shown in Table 3. The results indicate that Mesh 4 exhibits the lowest RMS error compared to all the other meshes examined, indicating its reliability in computation.

Table 3. Root mean square (RMS) error between the results obtained by the different meshes

RMS error	Mesh 1	Mesh 2	Mesh 3	Mesh 4
$x/h = -0.25$	0.168 720	0.144 850	0.152 740	0.129 670
$x/h = 0$	0.102 110	0.088 020	0.063 270	0.033 410
$x/h = 0.5$	0.076 361	0.072 303	0.068 134	0.042 460
$x/h = 1.0$	0.081 952	0.072 873	0.078 021	0.020 449

3. Results and discussion

3.1. Dynamic behavior

In order to achieve a thorough comprehension of the influence that coherent structures have on the efficiency of heat transfer, it is crucial to undertake a meticulous examination of the dynamic behavior exhibited by the flow through a diverse range of geometries, encompassing various Reynolds number ratios α. The precise identification of streamlines, turbulent parameters, and flow characteristics is pivotal in establishing a dependable correlation between the dynamic and heat field properties. The present study performed 3D steady simulations for three impinging jet geometries by utilizing the k–ω SST turbulence model, widely recognized for its precision in yielding accurate outcomes. Ansys Fluent was employed to solve the continuity, momentum and energy equations. The momentum and continuity equations were interdependent through the utilization of the SIMPLEC algorithm. The present study utilized the second-order upwind scheme and second-order central scheme for the calculation of various quantities and viscous terms, respectively. The PRESTO! (PREssure STaggering Option) methodology was employed to assess the face values of pressure terms.

3.2. Validation of the numerical simulation

To ensure the accuracy and reliability of the numerical model for the circular diffuser, a comparison was made between the computational results and the experimental data of Masip et al. [23], serving as a crucial validation step. Six locations were chosen to evaluate the implemented model, namely, $x/h = -0.75, -0.25, 0, 0.5, 0.75$ and 1, see Fig. 8. At the chosen axial locations, Fig. 7 illustrates the dimensionless velocity profiles for both the calculated numerical results and experimental data. Overall, the transverse flow velocity profiles calculated numerically show excellent agreement with the experimental data, with good correspondence observed
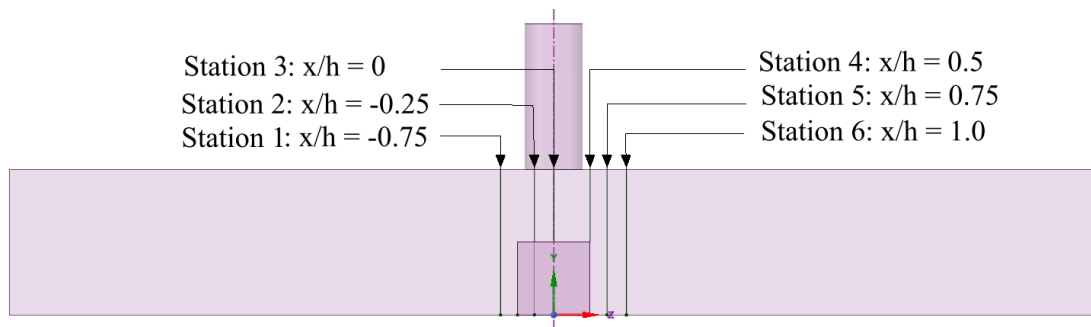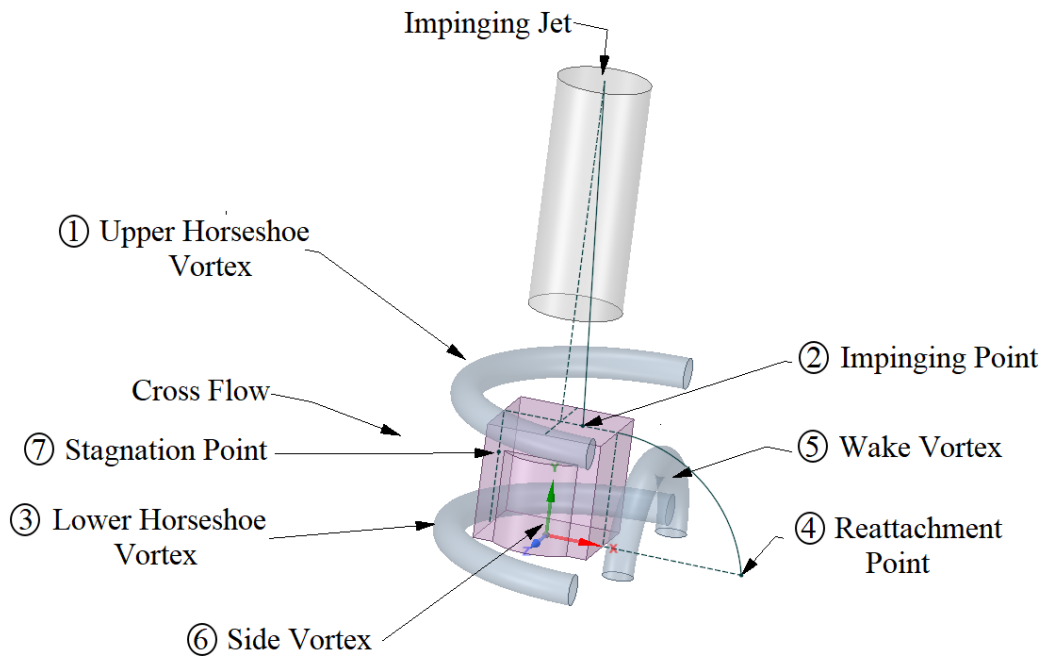

Fig. 8. Location of computing stations

Fig. 9. A schematic representation of the average flow patterns surrounding a component that is cooled by an impinging jet in a cross flow, as documented in reference [23]

at nearly all locations. It is noteworthy that the velocity profile exhibits negative values, indicating the presence of a reverse flow. The initial station ($x/h = -0.75$), positioned upstream of the cubic obstacle, exhibits flow acceleration in the upper portion of the channel due to the presence of the obstruction in the lower portion. The apex of the acceleration is observed at $y/h = 1.5$. Nonetheless, for the respective second, third, and fourth stations, the velocity of the fluid decelerates as it nears the diffuser jet. Upon traversing the cube, there is a discernible increase in the velocity of the liquid flow within the center of the channel. It should be noted that this augmentation reaches its peak values with respect to y/h at a value of 1. The k–ω SST model exhibited conformity with the anticipated pattern, albeit with marginal discrepancies for the initial station. Notwithstanding, the outcomes acquired for the remaining stations are in concordance with the empirical data, substantiating the soundness of the adopted model, mesh and parameters.

Fig. 9 highlights the flow patterns surrounding a cube that is being cooled by a jet that hits it in a cross direction. It specifically highlights the distinct vertical structures present in each of the four areas surrounding the component, which are the upper, frontal, wake, and side zones. According to Masip et al. [23], a cube exposed to a cross flow and impinging jet can generate consistent patterns known as coherent structures. An upper horseshoe vortex ① ensues in the upper zone as a result of the interplay between the cross flow and the radially flowing impinging jet that emanates from a jet impingement point ②. A retrograde flow phenomenon is observable in the vicinity of the downstream section of the hindmost surface, thereby, culminating at the reattachment point ④ and triggering the formation of a convoluted and curved vortex structure ⑤. The interaction between the channel flow and the lateral faces of the component results in the generation of a side vortex ⑥ in close proximity to each lateral face. A vortex in the shape of a horseshoe ③ positioned at the lower end of the channel and preceding the frontal surface is generated as a result of the interplay between the cross flow and the component. Fig. 10 shows the streamline contours within a plane at $z = 0$, which have been uniquely colored based
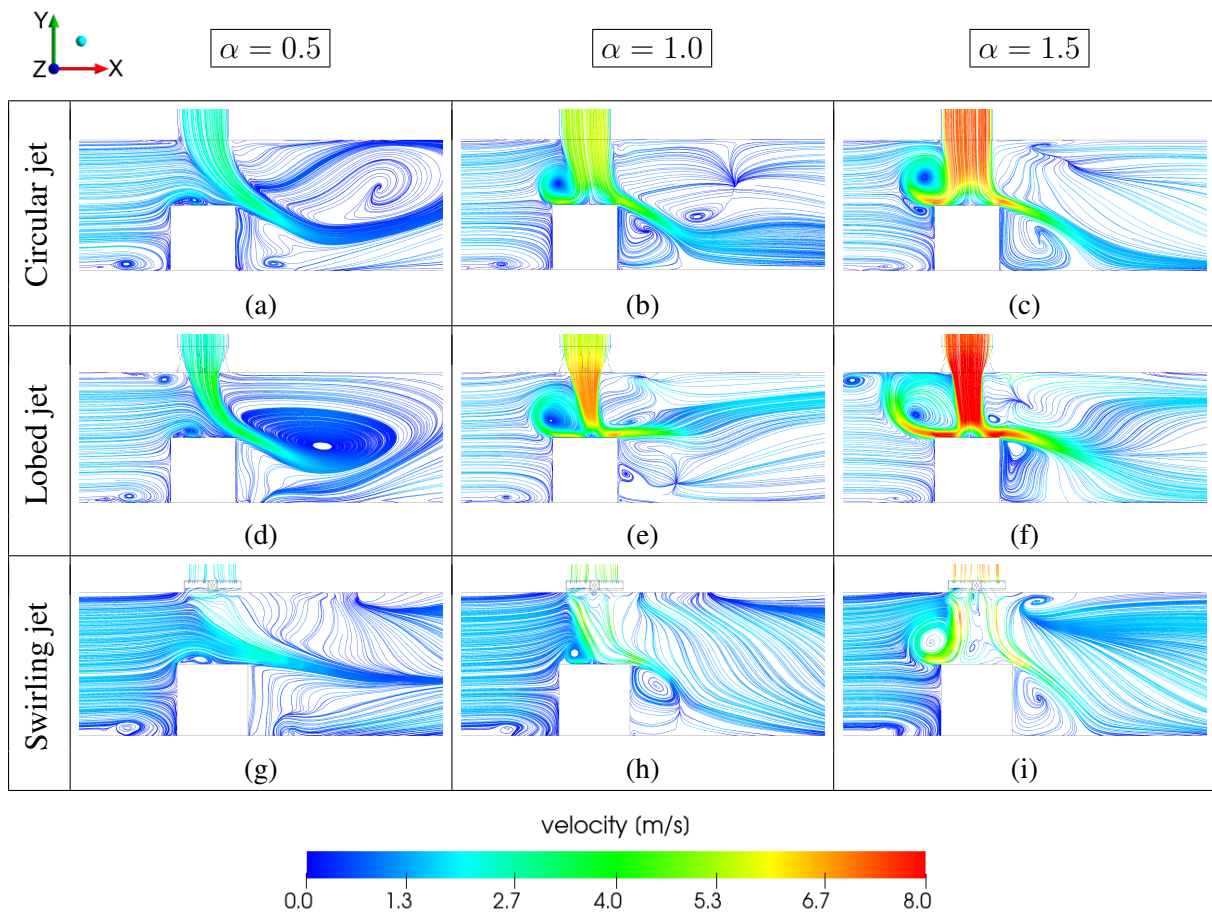
Fig. 10. Streamlines colored by the magnitude of the velocity in the $z = 0$ plane

on their velocity magnitude. This study reveals that the development of diverse flow fields is contingent upon the diffuser geometry and the ratio α.

There are two dominant characteristics that govern the fluid dynamics in the vicinity of the cube's upstream surface. The first characteristic, identified by Masip et al. in [23], is a stagnation point (marked as ⑦ in Fig. 9) on the upstream face of the cube at approximately $y/h = 0.7$. This point appears as a result of the interaction between the transverse flow and the upstream face of the cube. The second characteristic features a horseshoe-shaped vortex (lower horseshoe vortex (LHV), marked as ③ in Fig. 9), which is produced by the interaction between the transverse flow and the lower part of the cube.

In all three diffuser cases for $\alpha = 0.5$, the impinging jet did not reach the upper face of the cube as it was entrained by the transverse flow and deflected downstream of the cube. The shear layer separated and reattached downhill of the cube, creating a recirculation zone behind (Fig. 10a and d), particularly in the lobed jet. It should be noted that this zone is absent in the case of the swirling jet, which is due to the direction of the vanes of the swirling diffuser, which have the same direction as the cross flow, favoring the entrainment of the impinging jet by the cross flow (see Fig. 10g).

When the ratio of the Reynolds numbers of the impinging jet and the cross flow is unity (i.e., $\alpha = 1$), an impact zone appears on the upper face of the cube, which is due to the principal impinging jet related to the cross flow. In this case, a recirculation zone develops on the upper face of the cube called upper horseshoe vortex (marked as ① in Fig. 9), see Fig. 10e. Downstream
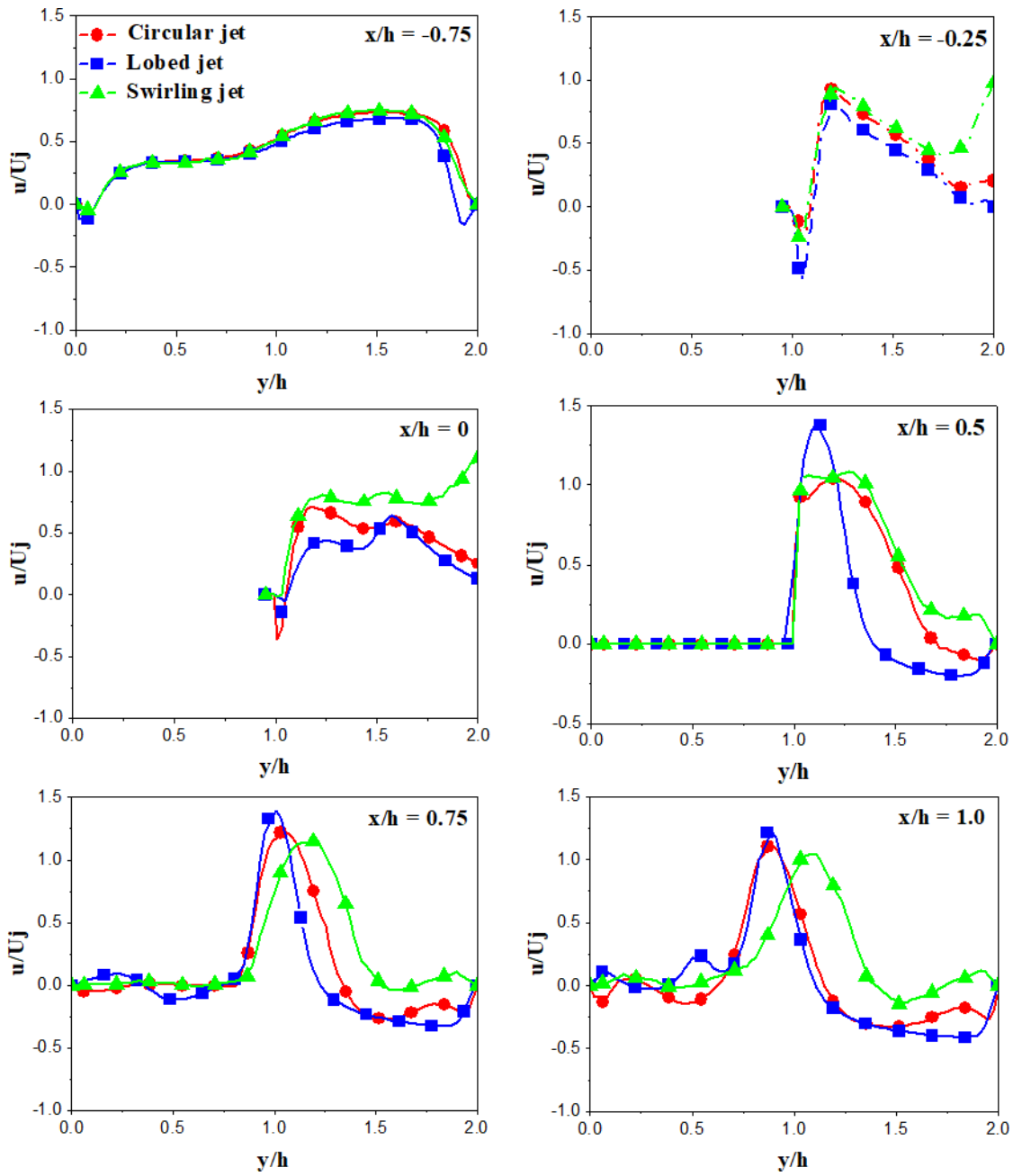
Fig. 11. Radial velocity profiles for the three geometries at selected axial locations with $z = 0$ and $\alpha = 0.5$

of the cube, flow separation leads to the formation of a recirculation zone in the wake region (wake vortex (WV), marked as ⑤ in Fig. 9). For $\alpha = 1.5$, the same recirculation zones marked as ① and ⑤ are observed in the previous cases but of larger sizes. The velocity profile shows a significant increase near the upper face of the cube for the lobed jet case, as depicted in Fig. 10f. In contrast, the increase in velocity is smaller for the circular and swirling cases, as shown in Fig. 10c and i, respectively. It is noteworthy that the maximum increase in velocity occurs in the proximity to the upper face of the cube for all the jet configurations. The recirculation zone (WV) located in the wake region is closer to the downstream face of the cube for the lobed jet case than the others, thus, ensuring proper cooling of the cube.

Figs. 11–13 show dimensionless radial velocity profiles u/U_j for the numerical results calculated for the three geometries (circular jet, lobed jet, and swirling jet) at the selected axial locations (Fig. 8). Each figure represents different stations relative to the center of the cube in the flow direction. These stations are used to show certain dynamic characteristics of the flow in each zone around the cube.

For the case of $\alpha = 0.5$ and the first station $x/h = -0.75$, which is located upstream of the cube, the radial velocity profiles at position $y/h = 0.2$ present negative velocities to form a small recirculation zone called LHV. For the three geometries at this station, the velocity in the direction of the current increases to reach its maximum value at $y/h = 1.5$. At the position $y/h = 1.8$, the effect of the upper horseshoe vortex (UHV) recirculation zone on the transverse flow is more significant in the case of the lobed jet.

At stations 2 and 3 ($x/h = -0.25$ and $x/h = 0$) at $z/h = 0$, the negative values of the velocity correspond to the region dominated by the top vortex (UHV, see Fig. 10a, d and g). However, if we consider stations 2, 3 and 4, the velocities increase in the flow direction to reach their maximum value at $y/h = 1.2$ for the three diffuser configurations. For the last stations 5 and 6, the flow accelerates in the central part of the channel with maximum values reported at the position $y/h = 1$, more visibly for the lobed jet, favoring thermal exchange. On the other hand, for the swirling jet, there is a radical shift for its maximum value under the influence of the fins fixed at the diffuser level, which have the same rotational direction as the transverse flow.

For the case of $\alpha = 1$, an impact zone appears on the top face of the cube due to the dominant impinging jet compared to the cross flow, located at the position $y/h = 1.25$. In this case, a UHV recirculation zone is more visible in the case of the lobed jet (see Fig. 12 with stations $x/h = -0.75$, -0.25 and 0). Behind the cube, flow separation leads to the formation of a recirculation zone in the wake region (WV) for all diffusers (see Fig. 12, stations $x/h = 0.75$ and 1.0 at positions $y/h = 0$ to 0.5). For stations $x/h = 0.5$, 0.75 and 1.0, the flow accelerates at the position $y/h = 1$ with maximum values due to the change in the canal section by the cube effect favoring the heat exchange between the flow and the cube. This phenomenon is visible for the case of the lobed jet, see Fig. 12.

At the stations $x/h = -0.75$ and -0.25 for the case of $\alpha = 1.5$, the velocities become negative at the position $y/h = 1$, indicating the existence of a UHV recirculation zone, which is more visible in the case of the lobed jet (see Fig. 13). For the station $x/h = 0$, this zone is absent for all diffuser configurations. For the stations $x/h = 0.5$, 0.75 and 1.0, the flow accelerates at the position $y/h = 1$ with maximum values due to the change in the channel section caused by the cube effect, favoring heat exchange between the flow and the cube. This phenomenon is visible for the lobed jet case (see Fig. 13).

In Fig. 14, the 3D vertical structures for the nine cases are displayed using the iso-surface of the Q-criterion and colored by velocity magnitude. The criterion, introduced by Hunt et al. in [14], is utilized to identify vortices and defined as follows:

$$Q = \frac{1}{2} \left(\|\Omega_{ij}\|^2 - \|S_{ij}\|^2 \right), \tag{15}$$

where Ω_{ij} is the antisymmetric vortex tensor

$$\Omega_{ij} = \frac{1}{2} \left(\frac{\partial U_i}{\partial x_j} - \frac{\partial U_j}{\partial x_i} \right). \tag{16}$$

If $Q > 0$, then a vortex is present, as the vortex tensor dominates the strain rate tensor. The
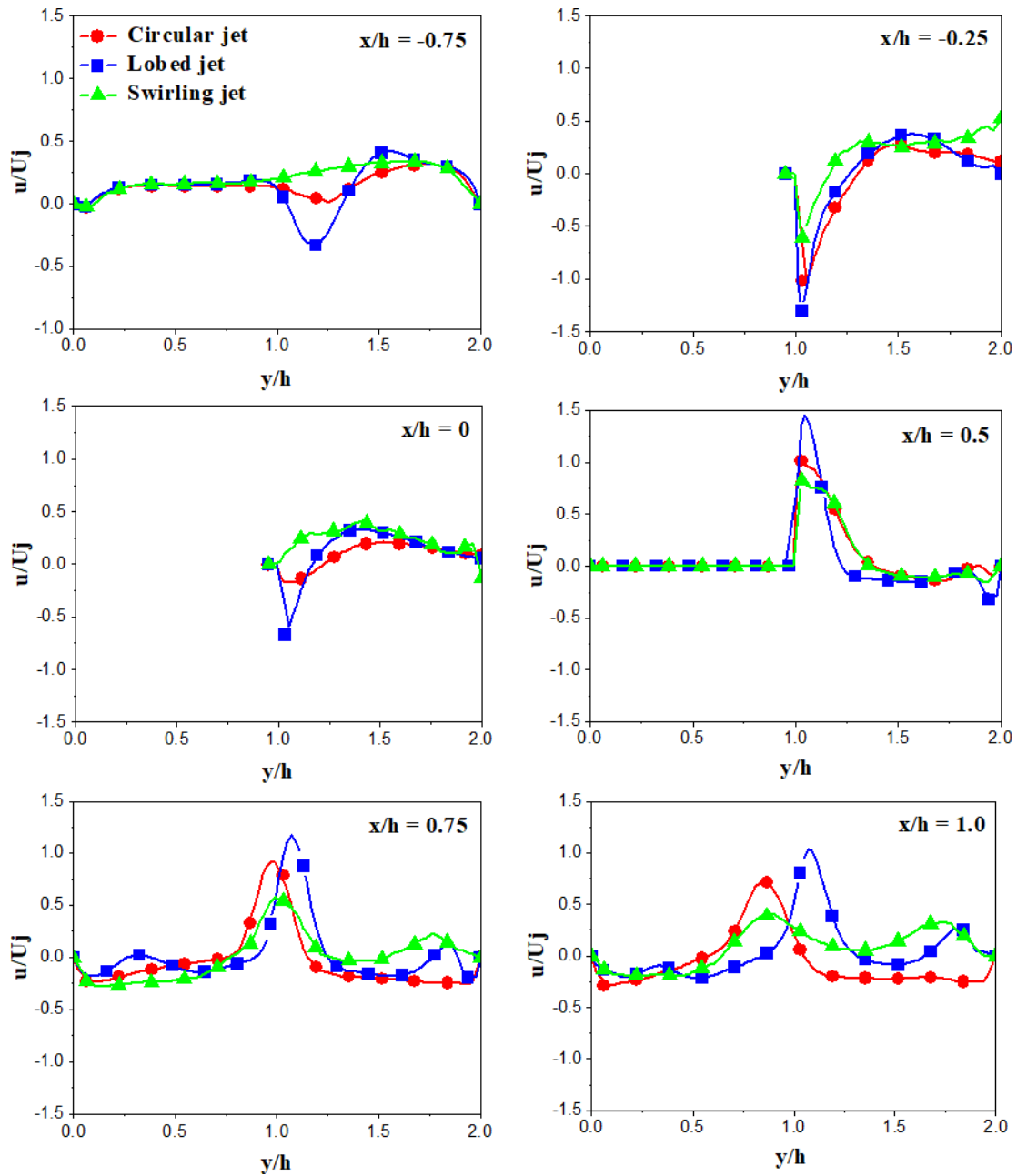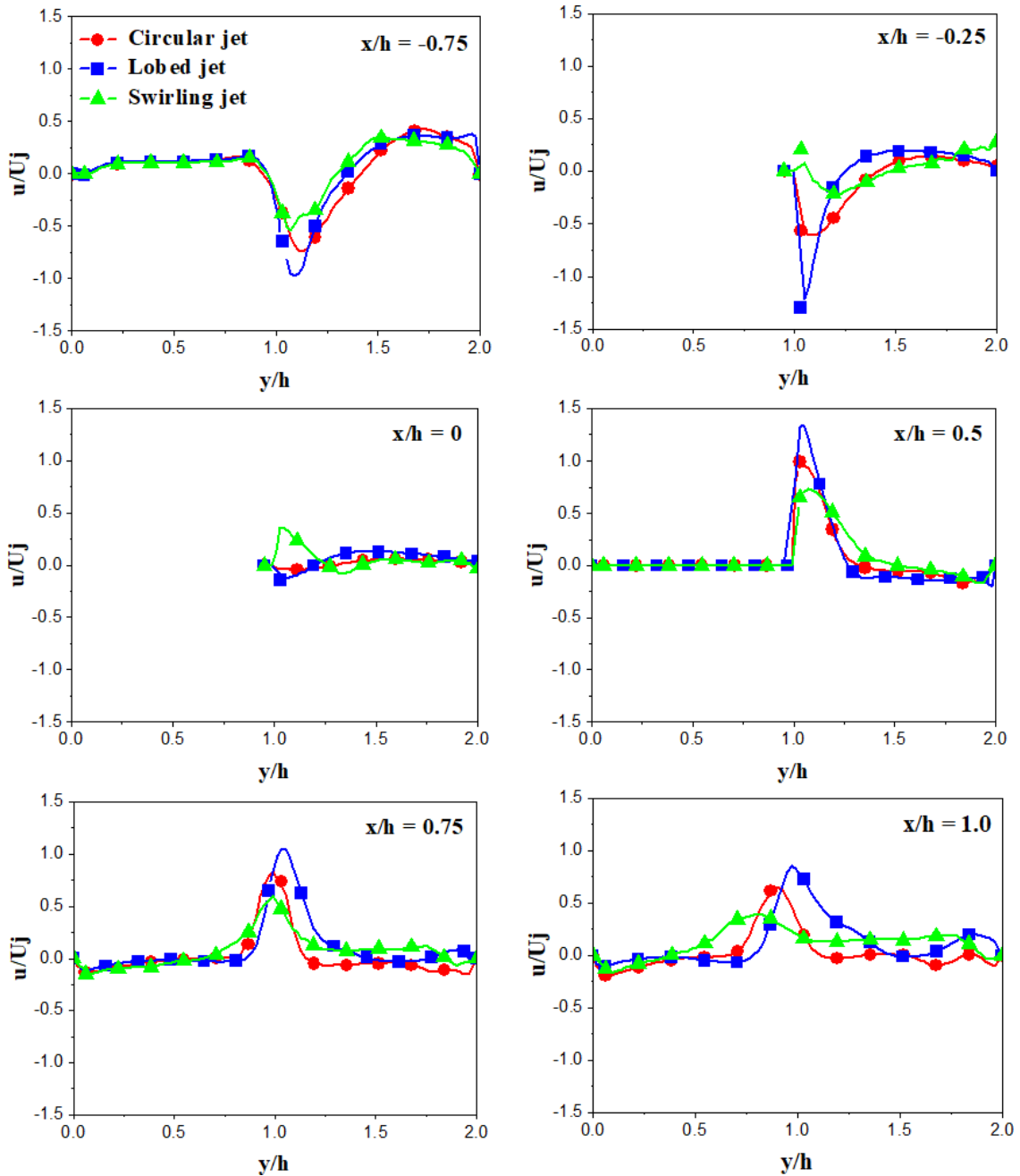
Fig. 12. Radial velocity profiles for the three geometries at selected axial locations with $z = 0$ and $\alpha = 1.0$

energy of the vortex can be measured by the magnitude of Q. The development of four vortices around the cubes is demonstrated by the plot of the iso-surface of Q.

Indeed, for $\alpha = 0.5$, the coherence structures are almost identical for the three diffuser configurations. Specifically, a superior horseshoe vortex (UHV) is produced due to the interaction between the transverse flow and the fluid moving radially from the jet. In the cases of the circular and swirling diffusers, the UHV size is almost the same, except for the lobed diffuser case, where it is larger due to the sweeping of the impacting jet upon the top surface of the cubic structure, which promotes good cooling. Moreover, the UHV size expands proportionally to the Reynolds number ratio augmentation. In close proximity to the lower wall of the conduit, a vortex in the shape of a horseshoe, referred to as the lower horseshoe vortex (LHV), arises

Fig. 13. Radial velocity profiles for the three geometries at selected axial locations with $z = 0$ and $\alpha = 1.5$

and continues to propagate in the downstream direction on both sides. This vortex is caused by the interaction between the transverse flow and the front face of the cube. In all diffuser configurations, the LHV size is almost the same.

Furthermore, for $\alpha = 1.5$, there is an interference between UHV and LHV, more noticeably for the lobed jet, accelerating the cube cooling. The flow pattern in the wake recirculation region is dominated by an arc-shaped vortex (WV) caused by the flow separation behind the cube. Another vortex (side vortex, SV) appears in the proximity of the lateral faces of the cube, which plays an important role in improving the cooling of these faces, especially in the lobed diffuser (see Fig. 14f).
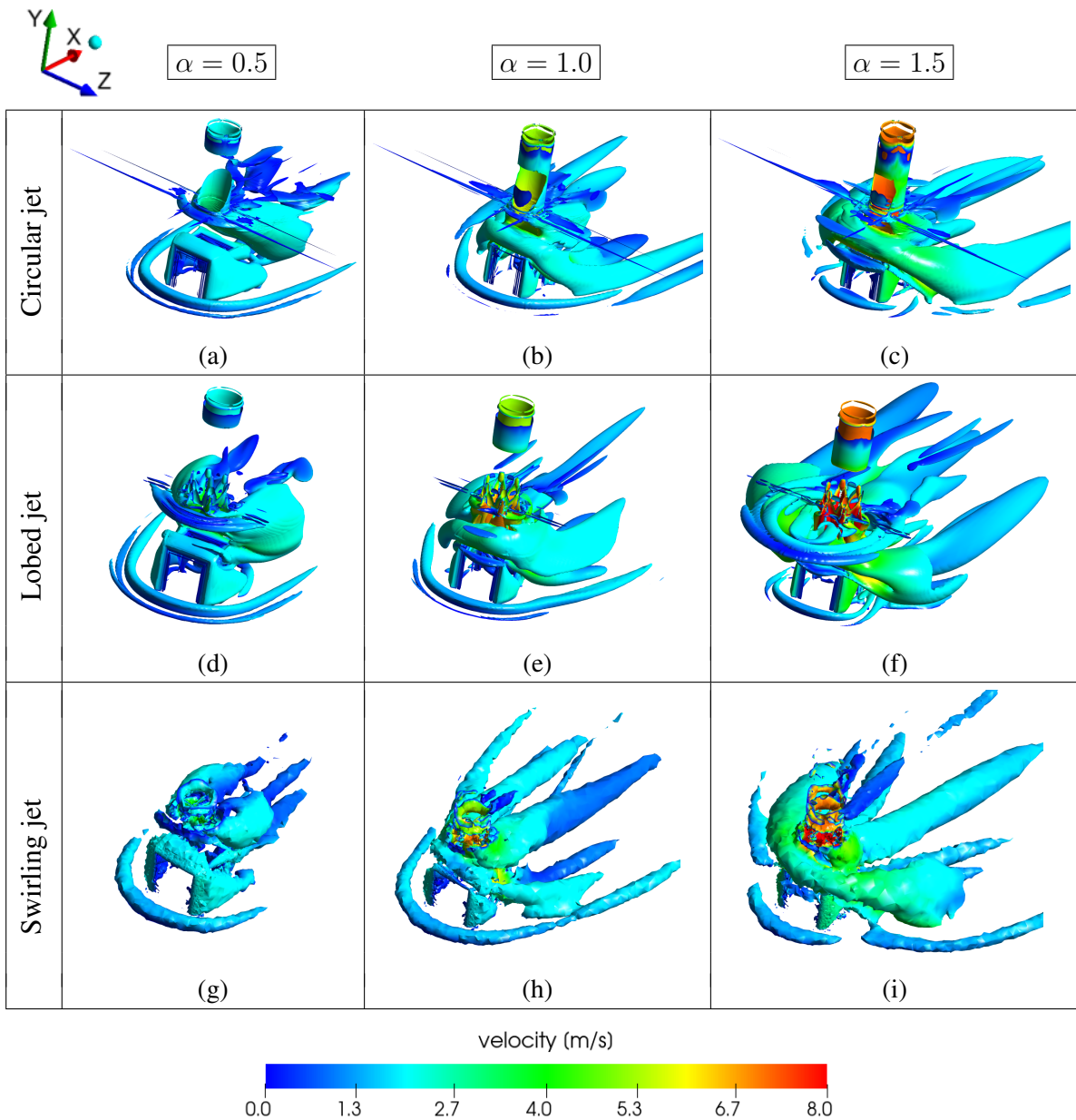
Fig. 14. Displays 3D vortical structures, visualized through the iso-surface of the Q-criterion (with $Q = 10^4 \, \mathrm{s}^{-2}$) and color-coded based on their velocity magnitude

3.3. Thermal behavior

The temperature field distribution is shown in Fig. 15 for the plane $z = 0$. From these figures, it can be observed that the temperature distribution is extended in the wake region of the cube for the case of $\alpha = 0.5$. A significant temperature increase is clearly visible in the vicinity of the heated walls of the cube for the lowest ratio case ($\alpha = 0.5$), and a less visible lower temperature is observed near the lateral walls for the high ratio cases ($\alpha = 1.0$ and 1.5). It is noted that for the lobed jet case at $\alpha = 0.5$ and $\alpha = 1.5$, there is a lower temperature near the lateral walls of the cube compared to the circular and swirling jet cases, thus, ensuring good cooling of the cube (see Fig. 15d). It was observed that the magnitude of the thermal boundary layer tends to diminish with the increase of the Reynolds number ratio α.
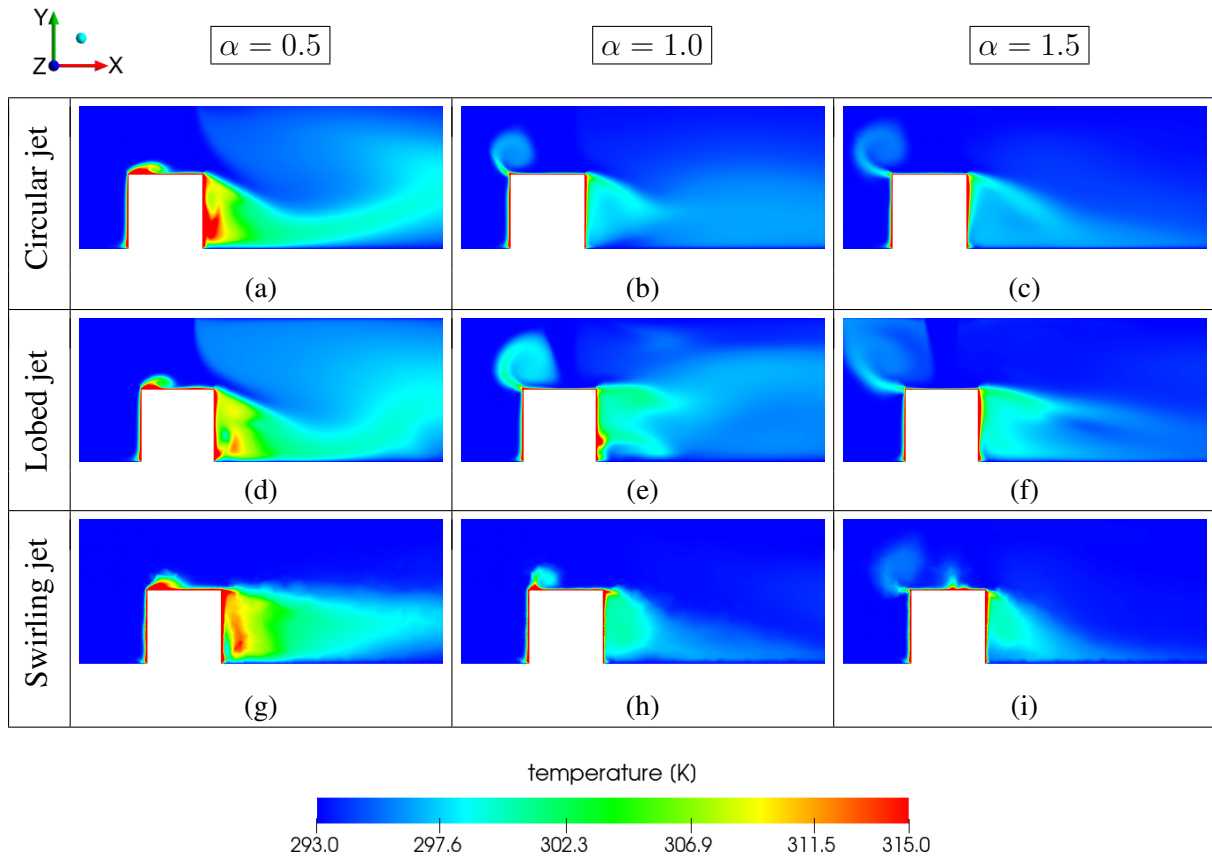
Fig. 15. Temperature contours in the plane $z = 0$

The contours of the local Nusselt number on the cube faces, folded out and projected on the plane, are shown in Fig. 16. It can be clearly seen that the Nusselt number increases as the impinging to cross flow ratio increases for all the geometries.

For $\alpha = 0.5$, almost the same contours of the Nusselt number are observed in the geometries of the circular and swirling jets, however, an appreciable enhancement in cooling efficiency is noted in the case of the lobed jet directed towards the upper cube face. On the front and upper faces of the cube, high values of the Nusselt number were obtained, implying good heat transfer on these faces. However, local hot spots are found on the lateral and rear faces, which may cause thermal stresses and material damage to electronic components.

When $\alpha = 1$, the cooling performance is improved, especially on the upper, lateral, and rear faces of the cube for all three geometries. A significant enhancement of heat flux is observed on the top face for the lobed and swirling jets due to the effect of the UHV developed on this cube face.

In the case of the highest Reynolds number ratio ($\alpha = 1.5$), the levels of the Nusselt number are higher than in the cases of $\alpha = 0.5$ and 1.0, therefore, the thermal exchange is improved on all faces of the cube. The upper face is the most enhanced zone by changing the diffuser geometry from circular to lobbed and swirl. Furthermore, by using the lobed diffuser, the heat transfer efficiency was improved significantly for the side face. Based on this finding, we can conclude that the lobed jet improved the cooling efficiency for the three Reynolds number ratios and we can state that there is a direct relationship between the flow morphology (type of diffuser) and the heat flux efficiency.

The distribution of the Nusselt number along the pathline ABCD, highlighted in Fig. 17,
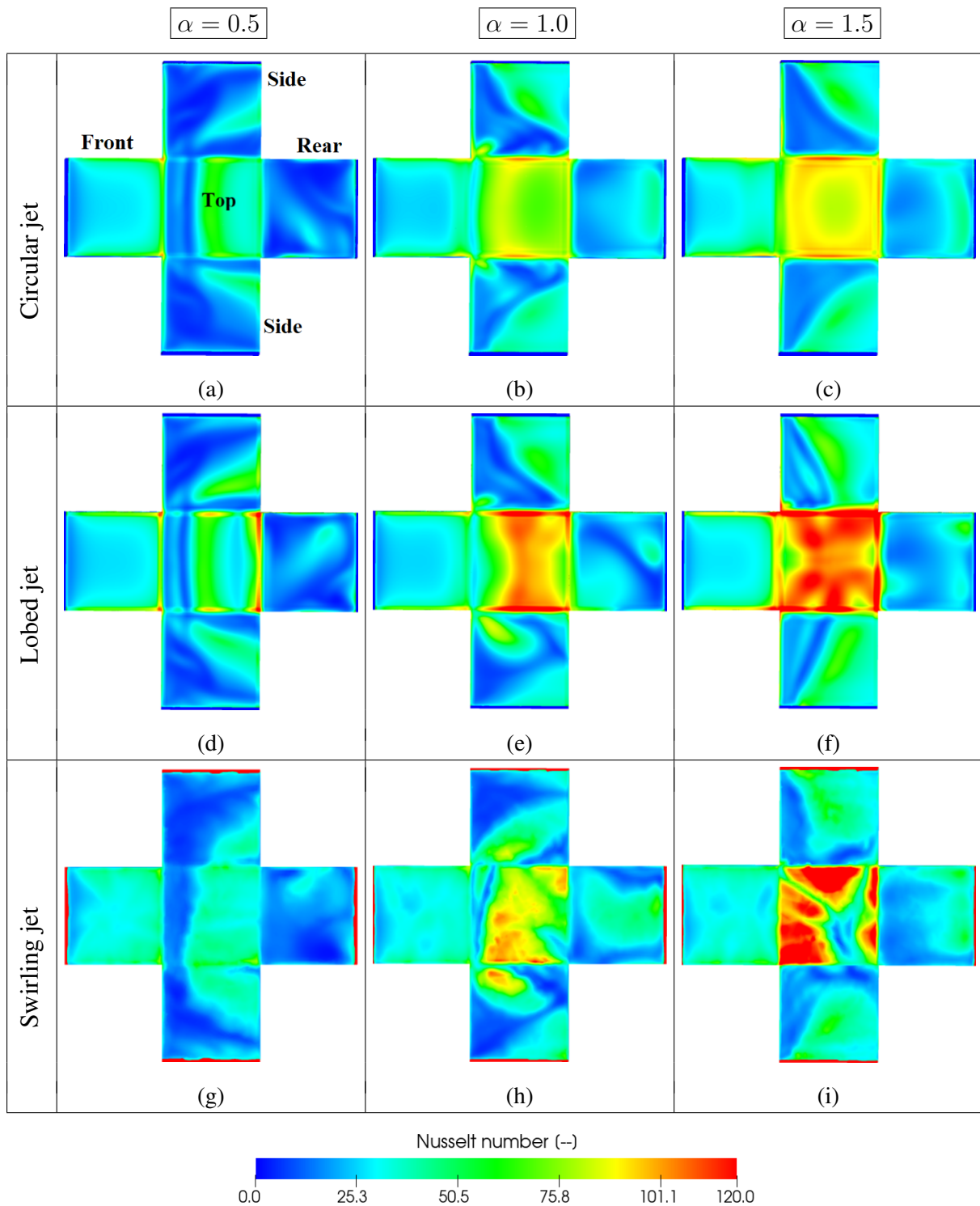
Fig. 16. Local Nusselt number contours on the cube faces for the three diffuser geometries

is displayed in Fig. 18. For all Reynolds number ratios, the profile of the Nusselt number is almost similar for the three geometries along the line [AB] located on the front face of the cube, with a slight improvement of convective heat transfer observed in the upper part of this face and more visibly for the lobed jet. This improvement in heat transfer results from the sweeping of cold air over the front face of the cube as shown in Fig. 10. For the top face of the cube (line
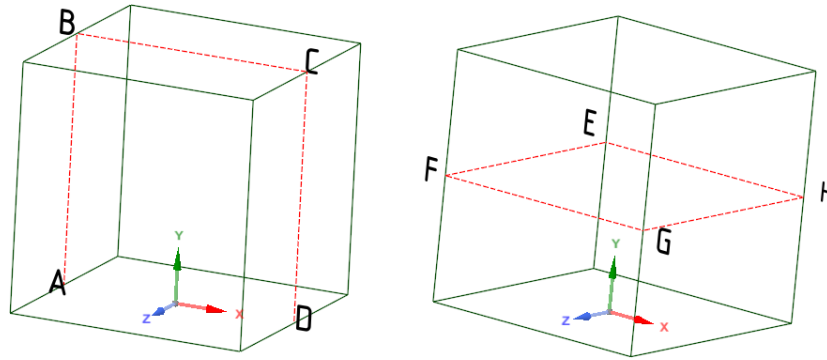
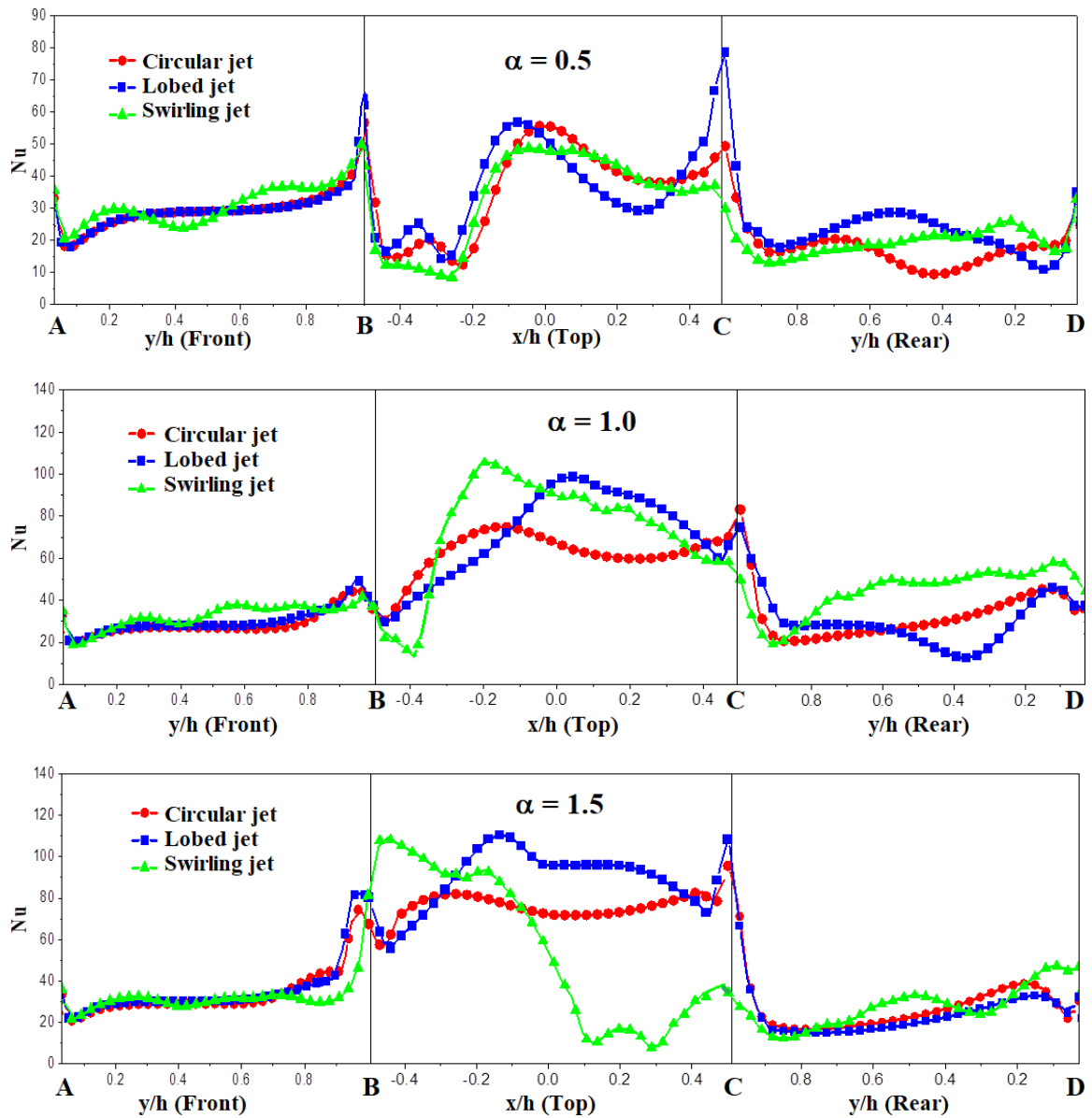Fig. 17. Placement of Nusselt number values along different lines

Fig. 18. Profiles of the Nusselt number along the pathline ABCD
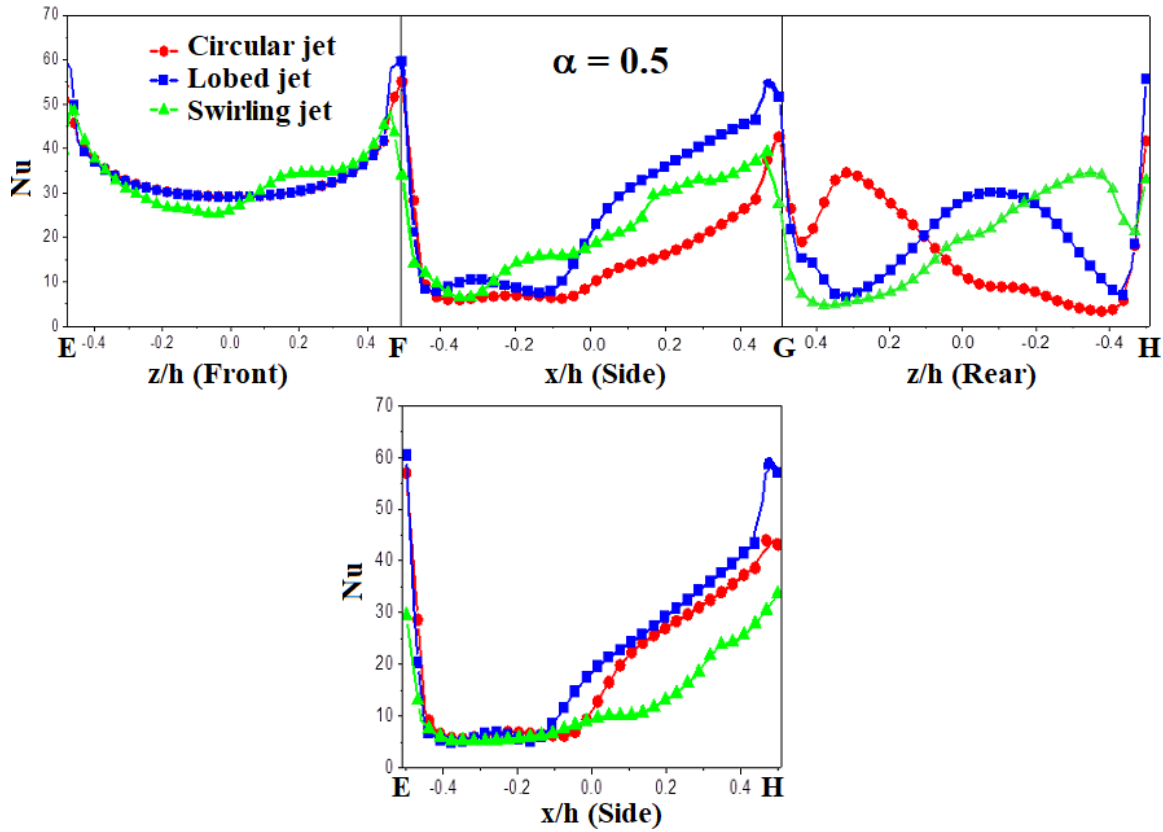
Fig. 19. Profiles of the Nusselt number along the pathline EFGHE with $\alpha = 0.5$

[BC]) and for all the geometries, a significant improvement in heat transfer is achieved when $\alpha = 1.0$ and 1.5, which can be explained by the production of the UHV. This improvement is more noticeable for the lobed jet, especially at $\alpha = 1.5$. A decrease in cooling efficiency is also observed at $x/h = 0.1$ to 0.3 on this face for the swirling jet geometry. For the line [CD], when $\alpha = 0.5$, a slight improvement in heat transfer is observed in the first part of the face for the lobed jet. When $\alpha = 1$, the swirling jet leads to better improvement of the cooling efficiency along this face. By increasing the ratio to $\alpha = 1.5$, the effect of changing the diffuser type on the heat transfer efficiency is not significant along this line.

Figs. 19–21 illustrate the variation in the Nusselt number along the pathline EFGHE, as depicted in Fig. 17. The Nusselt number trend along line [EF] remains similar for all three geometries along the front face of the cube, with a slight enhancement in heat transfer observed for the swirling jet. Notably, the rate of heat transfer increases near the edges and decreases at the center of the stagnation point on the faces. For $\alpha = 1.0$ and 1.5, the swirling jet geometry demonstrates a marginal improvement in cooling efficiency in the central part of the face. For the lateral face [FG], in the case of $\alpha = 0.5$, a better cooling improvement is achieved by the lobed diffuser geometry. For the ratio $\alpha = 1.0$, the heat exchange rate is increased for the circular jet geometry, especially in the middle part of this face. In the case of the highest ratio ($\alpha = 1.5$), the maximum Nusselt number is observed in the case of the lobed jet, thus, ensuring good cooling of this face. Along the line [GH], which corresponds to the back face of the cube, and for $\alpha = 0.5$, the heat transfer is increased in the central part of this face and more noticeably for the lobed jet. For the ratio $\alpha = 1.0$, the heat flux is increased for the swirling jet geometry, especially in the middle part of this face.
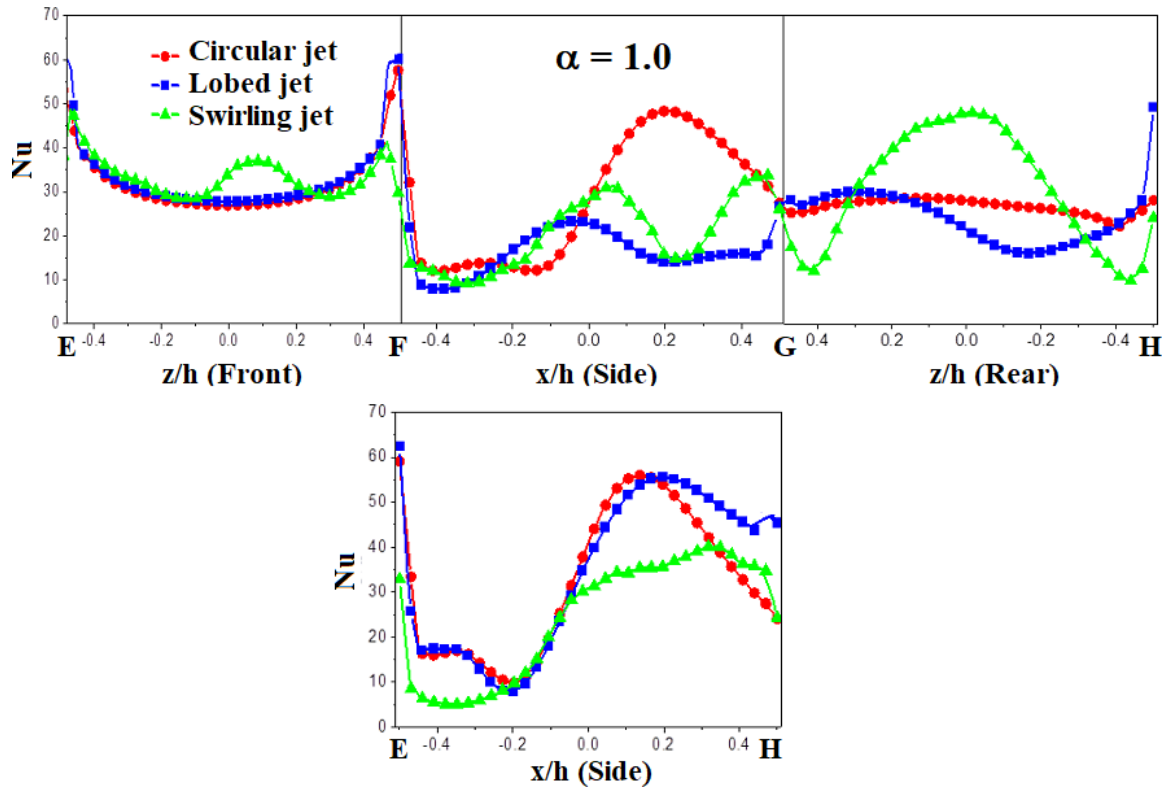
Fig. 20. Profiles of the Nusselt number along the pathline EFGHE with $\alpha = 1.0$
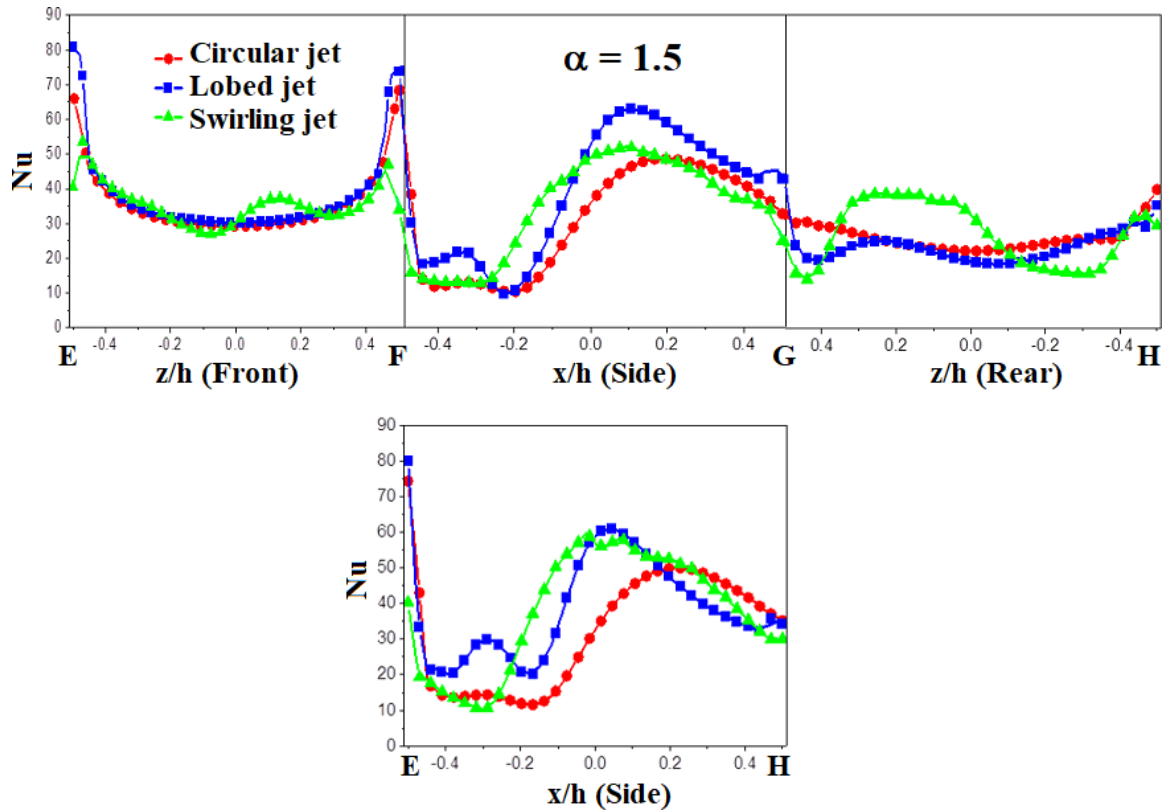

Fig. 21. Profiles of the Nusselt number along the pathline EFGH with $\alpha = 1.5$
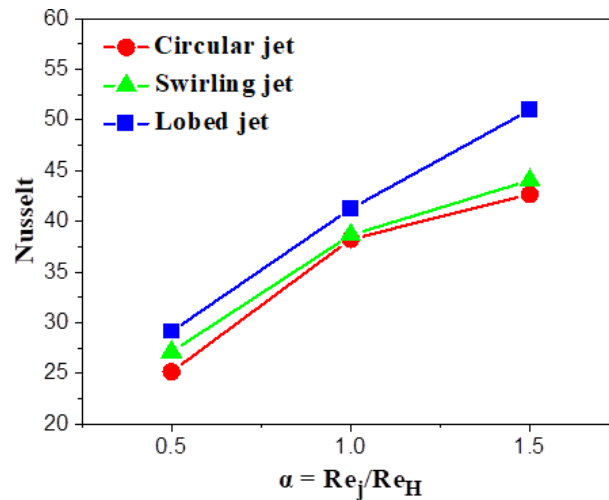
Fig. 22. Average Nusselt number as a function of the Reynolds number ratio

For the lateral face [EH], the effectiveness of cooling varies with the diffuser geometry and jet characteristics. When $\alpha = 0.5$, the lobed diffuser geometry demonstrates superior cooling performance. However, at $\alpha = 1.0$, the circular jet and lobed diffuser exhibit comparable heat exchange rates across this face, with a marginal enhancement in heat transfer noted for the swirl jet diffuser, particularly in the $x/h = [-0.5, -0.1]$ region. In the case of the highest ratio ($\alpha = 1.5$), the lobed jet stands out with the maximum Nusselt number, signifying excellent heat transfer. Moreover, the swirl jet diffuser, in this case, surpasses the circular jet, ensuring commendable cooling efficiency for the lateral face [EH].

The average Nusselt number as a function of the Reynolds number ratio α is presented in Fig. 22. The results clearly show that the overall Nusselt number increases with an increasing Reynolds number ratio. For $\alpha = 0.5$, both the swirling and lobed jet configurations exhibit a slight improvement in heat flux enhancement compared to the circular jet, with Nusselt number values of 27 and 29, respectively. However, for $\alpha = 1.0$, only the lobed configuration leads to an improvement in cooling efficiency, with an average Nusselt number of 41 representing a 7.3% improvement than the circular jet. At $\alpha = 1.5$, the lobed diffuser demonstrates the best cooling performance, with a Nusselt number of 51, which is more than 16.3 % compared to the circular jet.

4. Conclusions

The impact of modifying the jet diffuser geometry on the cooling efficiency of electronic components subjected to a transverse flow and an impinging jet was investigated through a numerical study using the k–ω SST model. The results showed that the adopted k–ω SST model reasonably predicted the average velocities in the streamwise direction when compared to experimental data. Additionally, it was demonstrated that increasing the Reynolds number ratio improved the heat flux for all diffuser geometries, while the flow characteristics and coherent structures, developed closer to the components, had a significant impact on wall heat transfer.

For the ratio $\alpha = 0.5$, the impinging jet did not reach the top face of the cube as it was entrained by the transverse flow and deflected downstream, producing a recirculation zone just behind the cube. For higher Reynolds number ratios $\alpha = 1.0$ and 1.5, the heat transfer was improved on all cube faces. For the swirl diffuser, a slight improvement in heat transfer of 7.2 %

and 3.2% was observed in the case of the Reynolds number ratios $\alpha = 0.5$ and $\alpha = 1.5$, respectively. The use of a lobed diffuser resulted in a substantial improvement in cooling efficiency across all three Reynolds number ratios. Specifically, the thermal efficiency was enhanced by more than 13.8% for $\alpha = 0.5$, 7.3% for $\alpha = 1.0$, and 16.3% for $\alpha = 1.5$, when compared to the circular diffuser. In conclusion, the lobed jet proved to be the most effective in terms of cooling efficiency for electronic components.

Acknowledgement

References

[1] Ajmi, M., Hnaien, N., Marzouk, S., Kolsi, L., Ghachem, K., Ben Aissia, H., Almeshaal, M. A., Numerical investigation of heat transfer enhancement of an inclined heated offset jet, International Communications in Heat and Mass Transfer 116 (2020) No. 104682. https://doi.org/10.1016/j.icheatmasstransfer.2020.104682

[2] Albayrak, M., Sarper, B., Saglam, M., Birinci, S., Aydin, O., The role of jet-to-crossflow velocity ratio on convective heat transfer enhancement in the cooling of discrete heating modules, Thermal Science and Engineering Progress 37 (2023) No. 101549. https://doi.org/10.1016/j.tsep.2022.101549

[3] Bahmani, M. H., Sheikhzadeh, G., Zarringhalam, M., Akbari, O. A., Al-Rashed, A. A. A. A., Shabani, G. A. S., Goodarzi, M., Investigation of turbulent heat transfer and nanofluid flow in a double pipe heat exchanger, Advanced Powder Technology 29 (2) (2018) 273–282. https://doi.org/10.1016/j.apt.2017.11.013

[4] Bedrouni, M., Khelil, A., Numerical study on the performance of rounded corners on the top of electronic components on cooling effectiveness, International Journal of Heat and Mass Transfer 150 (2020) No. 119391. https://doi.org/10.1016/j.ijheatmasstransfer.2020.119391

[5] Bennia, A., Fellouah, H., Khelil, A., Loukarfi, L., Naji, H., Experiments and large-eddy simulations of lobed and swirling turbulent thermal jets for HVAC's applications, Journal of Applied Fluid Mechanics 13 (1) (2020) 103–117. https://doi.org/10.29252/jafm.13.01.29970

[6] Bennia, A., Loukarfi, L., Braikia, M., Khelil, A., Naji, H., Experimental study of turbulent jet using lobed diffuser: Application to comfort in residential premises, Revue Nature and Technology 7 (2) (2015) 54–58. (in French)

[7] Bennia, A., Loukarfi, L., Khelil, A., Mohamadi, S., Braikia, M., Naji, H., Contribution to the experimental and numerical dynamic study of a turbulent jet issued from lobed diffuser, Journal of Applied Fluid Mechanics 9 (6) (2016) 2 957–2 967. https://doi.org/10.29252/jafm.09.06.25953

[8] Braikia, M., Naji, H., Khelil, A., Maammar, A., Experimental and CFD-based study of the interaction of lobed multi-jet diffusers in unbalanced positions, Journal of the Brazilian Society of Mechanical Sciences and Engineering 44 (7) (2022) No. 264. https://doi.org/10.1007/s40430-022-03570-3

[9] Choi, S.-K., Kim, S.-O., Turbulence modeling of natural convection in enclosures: A review, Journal of Mechanical Science and Technology 26 (1) (2012) 283–297. https://doi.org/10.1007/s12206-011-1037-0

[10] Choo, K., Kang, T. Y., Kim, S. J., The effect of inclination on impinging jets at small nozzle-to-plate spacing, International Journal of Heat and Mass Transfer 55 (13–14) (2012) 3 327–3 334. https://doi.org/10.1016/j.ijheatmasstransfer.2012.02.062

[11] Goodarzi, M., Safaei, M. R., Vafai, K., Ahmadi, G., Dahari, M., Kazi, S. N., Jomhari, N., Investigation of nanofluid mixed convection in a shallow cavity using a two-phase mixture model, International Journal of Thermal Sciences 75 (2014) 204–220.
https://doi.org/10.1016/j.ijthermalsci.2013.08.003

[12] Hearst, R. J., Gomit, G., Ganapathisubramani, B., Effect of turbulence on the wake of a wall-mounted cube, Journal of Fluid Mechanics 804 (2016) 513–530.
https://doi.org/10.1017/jfm.2016.565

[13] Huang, H., Sun, T., Zhang, G., Li, D., Wei, H., Evaluation of a developed SST k–ω turbulence model for the prediction of turbulent slot jet impingement heat transfer, International Journal of Heat and Mass Transfer 139 (2019) 700–712.
https://doi.org/10.1016/j.ijheatmasstransfer.2019.05.058

[14] Hunt, J. C. R., Wray, A. A., Moin, P., Eddies, streams, and convergence zones in turbulent flows, Proceedings of the Summer Program 1988, Center for Turbulence Research, 1988, pp. 193–208.

[15] Karabulut, K., Heat transfer improvement study of electronic component surfaces using air jet impingement, Journal of Computational Electronics 18 (4) (2019) 1 259–1 271.
https://doi.org/10.1007/s10825-019-01387-3

[16] Karabulut, K., Heat transfer increment study taking into consideration fin lengths for CuO-water nanofluid in cross flow-imping jet flow channels, Thermal Science 27 (6) (2023) 4 345–4 360.
https://doi.org/10.2298/TSCI221203035K

[17] Khan, B. A., Saha, A. K., Turbulent flow and heat transfer characteristics of an impinging jet over a heated wall-mounted cube placed in a cross-flow, Physics of Fluids 34 (2) (2022) No. 25120.
https://doi.org/10.1063/5.0079956

[18] Khelil, A., Naji, H., Braikia, M., Loukarfi, L., Comparative investigation on heated swirling jets using experimental and numerical computations, Heat Transfer Engineering 36 (1) (2015) 43–57. https://doi.org/10.1080/01457632.2014.906279

[19] Khelil, A., Naji, H., Loukarfi, L., Numerical study of swirling confined non-premixed flames with determination of pollutant emissions, International Review of Mechanical Engineering 1 (6) (2008).

[20] Khelil, A., Naji, H., Loukarfi, L., Meliani, M. H., Braikia, M., Numerical simulation of the interactions among multiple turbulent swirling jets mounted in unbalanced positions, Applied Mathematical Modelling 40 (5–6) (2016) 3 749–3 763. https://doi.org/10.1016/j.apm.2015.10.047

[21] Koseoglu, M. F., Baskaya, S., The effect of flow field and turbulence on heat transfer characteristics of confined circular and elliptic impinging jets, International Journal of Thermal Sciences 47 (10) (2008) 1 332–1 346. https://doi.org/10.1016/j.ijthermalsci.2007.10.015

[22] Lee, S. G., Experimental investigation of mixing-enhanced swirl flows, Journal of Mechanical Science and Technology 22 (12) (2008) 2 509–2 515. https://doi.org/10.1007/s12206-008-0910-y

[23] Masip, Y., Rivas, A., Larraona, G. S., Anton, R., Ramos, J. C., Moshfegh, B., Experimental study of the turbulent flow around a single wall-mounted cube exposed to a cross-flow and an impinging jet, International Journal of Heat and Fluid Flow 38 (2012) 50–71.
https://doi.org/10.1016/j.ijheatfluidflow.2012.07.004

[24] Menter, F. R., Review of the shear-stress transport turbulence model experience from an industrial perspective, International Journal of Computational Fluid Dynamics 23 (4) (2009) 305–316.
https://doi.org/10.1080/10618560902773387

[25] Meslem, A., Bode, F., Nastase, I., Martin, O., Optimization of lobed perforated panel diffuser: Numerical study of orifice geometry, Modern Applied Science 6 (12) (2012) 59–73.
https://doi.org/10.5539/mas.v6n12p59

[26] Meslem, A., Dia, A., Beghein, C., El Hassan, M., Nastase, I., Vialle, P.-J., A comparison of three turbulence models for the prediction of parallel lobed jets in perforated panel optimization, Building and Environment 46 (11) (2011) 2 203–2 219.
https://doi.org/10.1016/j.buildenv.2011.04.037

[27] Meslem, A., Nastase, I., Abed-Meraim, K., Experimental investigation of the mixing performance of a lobed jet flow, Journal of Engineering Physics and Thermophysics 81 (1) (2008) 106–111. https://doi.org/10.1007/s10891-008-0006-7

[28] Ostheimer, D., Yang, Z., A CFD study of twin impinging jets in a cross-flow, The Open Numerical Methods Journal 4 (1) (2012) 24–34. https://doi.org/10.2174/1876389801204010024

[29] Podila, K., Rao, Y., CFD modelling of supercritical water flow and heat transfer in a 2×2 fuel rod bundle, Nuclear Engineering and Design 301 (2016) 279–289. https://doi.org/10.1016/j.nucengdes.2016.03.019

[30] Popovac, M., Hanjalić, K., Large-eddy simulations of flow over a jet-impinged wall-mounted cube in a cross stream, International Journal of Heat and Fluid Flow 28 (6) (2007) 1 360–1 378. https://doi.org/10.1016/j.ijheatfluidflow.2007.05.009

[31] Rakhsha, S., Zargarabadi, M. R., Saedodin, S., The effect of nozzle geometry on the flow and heat transfer of pulsed impinging jet on the concave surface, International Journal of Thermal Sciences 184 (2023) No. 107925. https://doi.org/10.1016/j.ijthermalsci.2022.107925

[32] Rundström, D., Moshfegh, B., Investigation of flow and heat transfer of an impinging jet in a cross-flow for cooling of a heated cube, Journal of Electronic Packaging 128 (2) (2006) 150–156. https://doi.org/10.1115/1.2188948

[33] Safaei, M. R., Togun, H., Vafai, K., Kazi, S. N., Badarudin, A., Investigation of heat transfer enhancement in a forward-facing contracting channel using FMWCNT nanofluids, Numerical Heat Transfer, Part A: Applications 66 (12) (2014) 1 321–1 340. https://doi.org/10.1080/10407782.2014.916101

[34] Saleha, N., Fadèla, N., Abbès, A., Improving cooling effectiveness by use of chamfers on the top of electronic components, Microelectronics Reliability 55 (7) (2015) 1 067–1 076. https://doi.org/10.1016/j.microrel.2015.04.006

[35] Tatsumi, K., Tanaka, M., Woodfield, P. L., Nakabe, K., Swirl and buoyancy effects on mixing performance of baffle-plate-type miniature confined multijet, International Journal of Heat and Fluid Flow 31 (1) (2010) 45–56. https://doi.org/10.1016/j.ijheatfluidflow.2009.09.005

[36] Thundil Karuppa Raj, R., Ganesan, V., Study on the effect of various parameters on flow development behind vane swirlers, International Journal of Thermal Sciences 47 (9) (2008) 1 204–1 225. https://doi.org/10.1016/j.ijthermalsci.2007.10.019

[37] Togun, H., Safaei, M. R., Sadri, R., Kazi, S. N., Badarudin, A., Hooman, K., Sadeghinezhad, E., Numerical simulation of laminar to turbulent nanofluid flow and heat transfer over a backward-facing step, Applied Mathematics and Computation 239 (2014) 153–170. https://doi.org/10.1016/j.amc.2014.04.051

[38] Tummers, M. J., Flikweert, M. A., Hanjalić, K., Rodink, R., Moshfegh, B., Impinging jet cooling of wall mounted cubes, Engineering Turbulence Modelling and Experiments 6 (2005) 773–782. https://doi.org/10.1016/B978-008044544-1/50074-1

[39] Vassighi, A., Sachdev, M., Thermal and power management of integrated circuits, IEEE Transactions on Device and Materials Reliability 6 (2) (2006) 300–305. https://doi.org/10.1109/TDMR.2006.876577

[40] Wang, C., Luo, L., Wang, L., Sundén, B., Effects of vortex generators on the jet impingement heat transfer at different cross-flow Reynolds numbers, International Journal of Heat and Mass Transfer 96 (2016) 278–286. https://doi.org/10.1016/j.ijheatmasstransfer.2016.01.042

[41] Wilcox, D. C., Reassessment of the scale-determining equation for advanced turbulence models, AIAA Journal 26 (11) (1988) 1 299–1 310. https://doi.org/10.2514/3.10041

[42] Xu, K., Wang, G., Wang, L., Yun, F., Sun, W., Wang, X., Chen, X., CFD-Based study of nozzle section geometry effects on the performance of an annular multi-nozzle jet pump, Processes 8 (2) (2020) No. 133. https://doi.org/10.3390/pr8020133